

*Annual Review of Chemical and Biomolecular
Engineering*

Liquid-Phase Transmission
Electron Microscopy for
Reliable In Situ Imaging of
Nanomaterials

Jongbaek Sung,^{1,2,*} Yuna Bae,^{1,2,*} Hayoung Park,^{1,2}
Sungsu Kang,^{1,2} Back Kyu Choi,^{1,2} Joodeok Kim,^{1,2}
and Jungwon Park^{1,2,3,4}

¹School of Chemical and Biological Engineering, and Institute of Chemical Processes, Seoul National University, Seoul, Republic of Korea; email: hyde217@snu.ac.kr, yunabae@snu.ac.kr, julia0184@snu.ac.kr, sung sukang@snu.ac.kr, chlqorrb122@snu.ac.kr, juori22@snu.ac.kr, jungwonpark@snu.ac.kr

²Center for Nanoparticle Research, Institute for Basic Science (IBS), Seoul, Republic of Korea

³Institute of Engineering Research, College of Engineering, Seoul National University, Seoul, Republic of Korea

⁴Advanced Institutes of Convergence Technology, Seoul National University, Gwanggyo-ro, Yeongtong-gu, Suwon-si, Gyeonggi-do, Republic of Korea

Annu. Rev. Chem. Biomol. Eng. 2022. 13:167–91

The *Annual Review of Chemical and Biomolecular Engineering* is online at chembioeng.annualreviews.org

<https://doi.org/10.1146/annurev-chembioeng-092120-034534>

Copyright © 2022 by Annual Reviews.
All rights reserved

*These authors contributed equally to this article

Keywords

liquid-phase transmission electron microscopy, in situ characterization, nanomaterial, electron-beam control, atomic-scale analysis, machine-learning data analysis

Abstract

Liquid-phase transmission electron microscopy (LPTEM) is a powerful in situ visualization technique for directly characterizing nanomaterials in the liquid state. Despite its successful application in many fields, several challenges remain in achieving more accurate and reliable observations. We present LPTEM in chemical and biological applications, including studies for the morphological transformation and dynamics of nanoparticles, battery systems, catalysis, biomolecules, and organic systems. We describe the possible interactions and effects of the electron beam on specimens during observation and present sample-specific approaches to mitigate and control these electron-beam effects. We provide recent advances in achieving atomic-level resolution for liquid-phase investigation of structures and

**ANNUAL
REVIEWS CONNECT**

www.annualreviews.org

- Download figures
- Navigate cited references
- Keyword search
- Explore related articles
- Share via email or social media

dynamics. Moreover, we discuss the development of liquid cell platforms and the introduction of machine-learning data processing for quantitative and objective LPTEM analysis.

1. INTRODUCTION

The liquid phase serves as a native environment for many material and chemical reactions. In liquids, solvent molecules dynamically interact with suspended materials, evolving unique structural characteristics that are closely related to their function (1, 2). Furthermore, many fundamental reactions, including syntheses, phase transformations, and surface reactions, occur in liquids. Precisely controlling these reactions can substantially improve the fields of catalysis, sensing, coating, and energy applications. Therefore, an analytical method that enables in situ investigation of material structures and dynamics in liquid can provide both fundamental and practical insights for chemistry, physics, and biology.

Liquid-phase transmission electron microscopy (LPTEM) is a promising tool that provides sufficient temporal and spatial resolution to investigate liquid-phase chemical events in situ (3–5). In LPTEM, liquid specimens are hermetically sealed in a nano-sized cell and safely introduced into transmission electron microscopy (TEM). The overall thickness of the liquid cell is typically less than a few hundred nanometers, enabling LPTEM to maintain the high resolution of conventional TEM. Combined with state-of-the-art TEM detectors (6, 7), LPTEM can capture liquid-phase chemical events at less than subnanometer and millisecond resolutions.

Since its first demonstration in 2003 (8), LPTEM has uncovered the underlying mechanisms of various liquid-phase chemical phenomena. For example, morphological changes in inorganic nanomaterials such as growth, etching, and assembly have been studied intensively via LPTEM (9). With the development of microelectromechanical systems, external stimuli including liquid flow, electrical bias, and heating have been successfully implemented to study electrochemical and catalytic systems via LPTEM. The intrinsic structures and dynamics of soft materials, such as synthetic polymers, metal-organic frameworks (MOFs), and biomolecules, have also been observed directly via LPTEM (10).

LPTEM has helped resolve fundamental questions of chemistry and biology, and further advances in LPTEM technology to provide more precise and reliable examinations are underway. The high-energy electron beam of TEM can potentially alter a liquid from its intact state. Therefore, minimizing the electron-beam effect or exploiting it to induce the chemical reaction of interest is of utmost importance in the current LPTEM field. Moreover, LPTEM must provide subnanometer- or atomic-level information on material structure and dynamics for efforts to engineer material structures at the atomic level. Finally, development of methods that ensure reproducible imaging conditions and unprejudiced data interpretation can further improve LPTEM.

Herein, we elucidate LPTEM's contribution to the fields of chemical and biological engineering and highlight recent advances in LPTEM that address the aforementioned challenges. After introducing the LPTEM technique and its applications, we present efforts to manipulate the electron beam during LPTEM investigation to either suppress unwanted reactions or stimulate desired reactions. We also discuss LPTEM studies to resolve material structure and dynamics at the near-atomic scale. Finally, we introduce advanced LPTEM designs and automated data analysis for quantitative and objective LPTEM.

2. LIQUID-PHASE TRANSMISSION ELECTRON MICROSCOPY: METHODS AND APPLICATIONS

TEM is a high-resolution microscopic method using an electron beam. In TEM, the electron beam is generally accelerated with a voltage of 60–300 kV, shortening its wavelength to a few picometers. Consequently, the maximum achievable resolution of the microscope also reduces to a sub-angstrom level (11). The accelerated electron beam is focused on the specimen and scattered by the individual atoms during transmission. The scattering results in a phase shift of the electron beam, which contains information about the local charge density of the specimen.

To minimize electron-beam scattering other than that of the specimen, ultrahigh-vacuum conditions ($<10^{-4}$ Pa) must be maintained in TEM. However, liquid evaporation could easily break the ultrahigh-vacuum conditions. Along with the evaporated molecules, the liquid specimen itself and the liquid-encapsulating materials can all cause multiple scattering and deteriorate the image resolution (4, 12, 13). Therefore, sample loading methods that can completely enclose a liquid sample with minimal thickness are required to realize LPTEM.

With the development of microfabrication and thin-film technologies, modern LPTEM uses a closed-cell approach to safely seal liquid specimens while achieving minimal resolution loss. A liquid specimen is sandwiched between two windows with an overall thickness typically below a few hundred nanometers. Mechanically strong, electron beam-transparent materials such as SiN_x graphene are used as windows (8, 14). Because the window is composed of light elements with thicknesses typically less than 50 nm, the unwanted electron-beam scattering by the window is minimized.

Commercial LPTEM platforms are based on Si-chips with tens-of-nanometers-thick SiN_x windows (8) (**Figure 1a**). In general, the liquid specimen is enclosed by two Si/ SiN_x chips, with SiN_x windows vertically aligned to provide a path for the electron beam. In addition, a metal spacer or an O-ring is installed to ensure complete sealing and to control liquid thickness. A spatial resolution of nanometer scale is easily achievable in this platform, owing to the reduced thickness of windows and the encapsulated liquid. The Si/ SiN_x platform can micropattern sophisticated architectures, including fluid channels, electrodes, and heating elements in the liquid cell, enabling operando LPTEM studies. A closed liquid cell using two sheets of graphene (graphene liquid cell, or GLC) provides notably high spatial resolution compared to the Si/ SiN_x platform owing to its few-atom-thick window (14, 15) (**Figure 1b**). Given its high mechanical strength, high impermeability, and strong interlayer interaction, graphene can perfectly encapsulate liquid specimens without need of spacer material (16, 17). Although GLC lacks commercial availability, its fabrication could be performed easily in the laboratory and imaged with a conventional TEM holder (18). Furthermore, installation of an external stimuli such as liquid flow in GLC has been demonstrated recently (19). We also note that a low-vapor pressure liquid (e.g., ionic liquid) can withstand the vacuum conditions of TEM, thus allowing observation without any encapsulation methods (20) (**Figure 1c**). Although this open cell approach has limited liquid choices, it provides spatial resolution similar to that of dry-state TEM.

LPTEM continuously records the dynamic processes of nanomaterials in their native conditions, whereas other TEM-based methods, such as dry-state TEM and cryogenic TEM (cryo-TEM), can capture only snapshots of nanomaterials in a dried or vitrified state. Moreover, conventional TEM-based analyses, specifically electron diffraction, high-resolution imaging, energy dispersive X-ray spectroscopy (EDS), and electron energy loss spectroscopy (EELS), are readily compatible during LPTEM imaging. In the following sections, we briefly summarize the contributions of LPTEM in various fields of chemical and biological engineering.

2.1. Nanoparticle Growth

Understanding nanomaterial growth is essential for controlling property-related structural characteristics, such as size, morphology, and atomic arrangements of nanomaterials. LPTEM has been used consistently to observe nanoparticle growth mechanisms (8, 9, 21). The electron beam was used to create a liquid environment that contained highly reductive species (Section 3.1), which induced nanoparticle growth from the precursor solution (22). Consequently, the growth dynamics of various metal nanoparticles were visualized successfully via LPTEM (23–27). The results demonstrated that nonclassical growth processes coexisted with the classical growth process of monomer attachment (28). For example, direct observation of Pt nanoparticle growth revealed

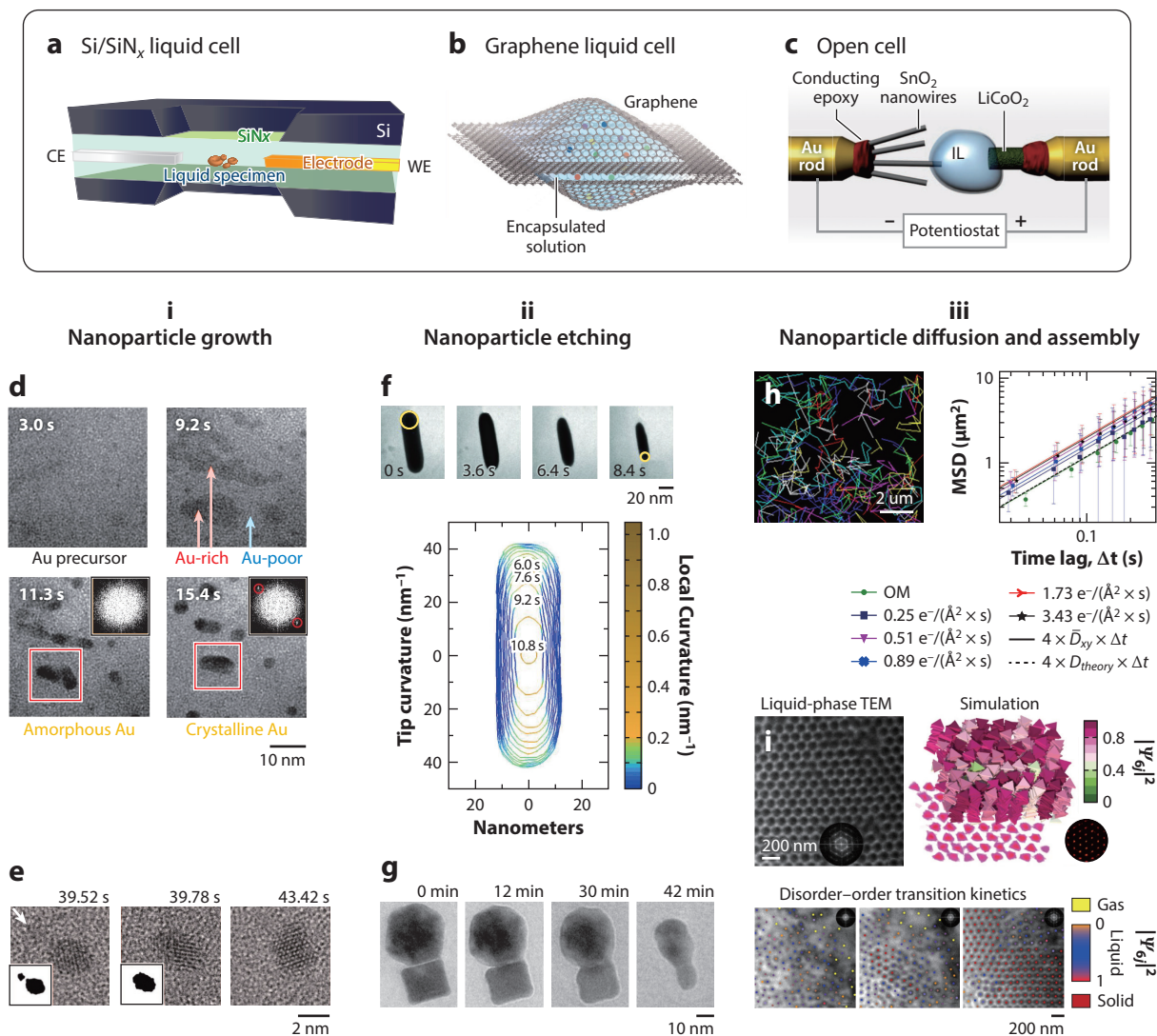


Figure 1

(Continued)

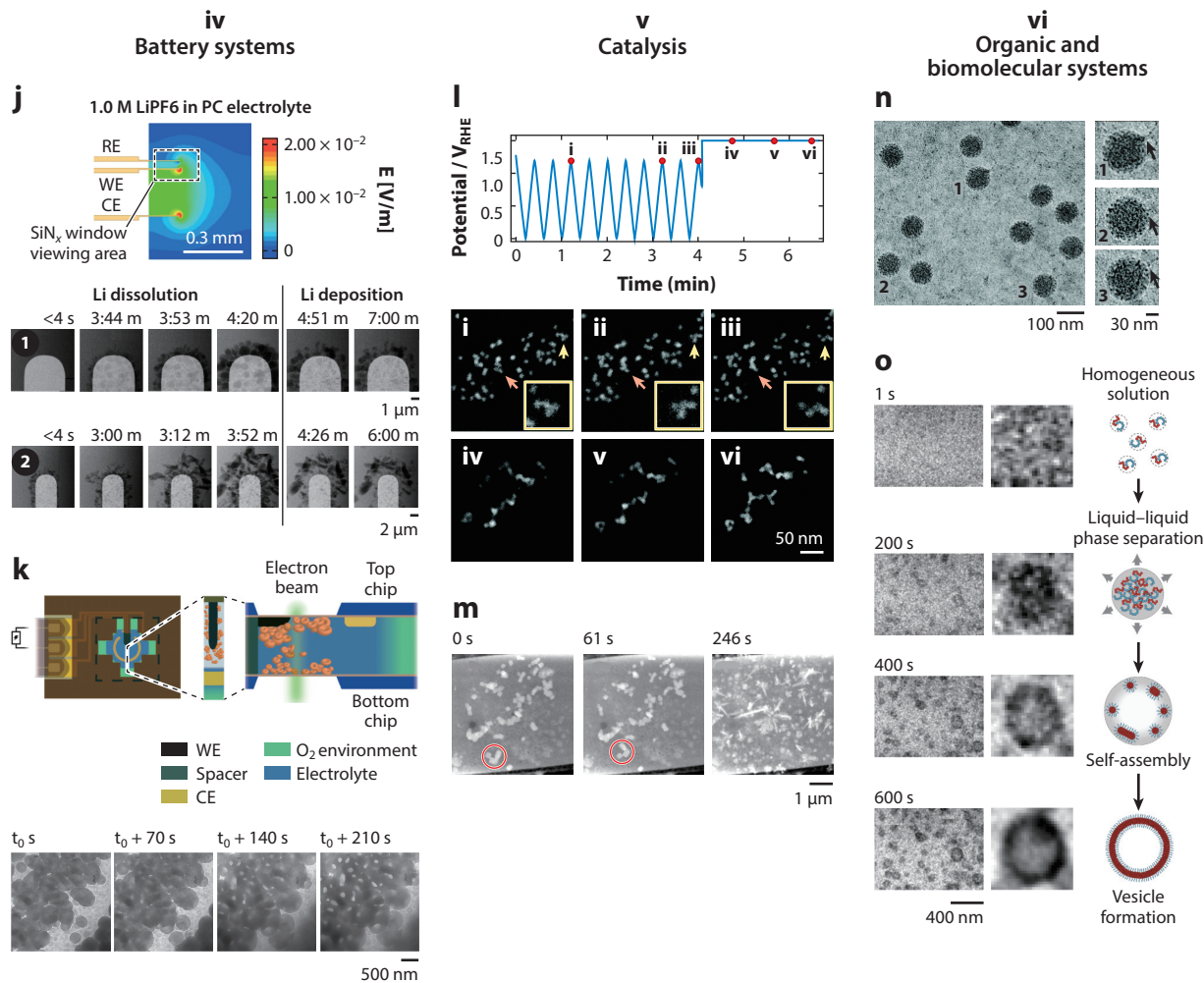


Figure 1

(*a-c*) Schematic illustration of a (*a*) Si/SiN_x platform, (*b*) graphene liquid cell, and (*c*) open cell platform for LPTEM. (*d*) Nonclassical growth pathway of Au nanoparticles including spinodal decomposition, nucleation, and crystallization. (*e*) Nonclassical growth pathway of a Pt nanoparticle via coalescence. (*f*) Formation of high-index surfaces during kinetically driven etching of a Au nanorod. (*g*) Local-site-specific etching trajectory of a Pt icosahedron and nanocube. (*h*) Brownian motion of nanoparticles observed in LPTEM. (*i*) Three-dimensional self-assembly of Au nanoprisms in LPTEM (*top*) and disorder-to-order transition during self-assembly (*bottom*). (*j*) Electric field distribution in the electrochemical LPTEM and Li plating/stripping dynamics during the first and second cycles. (*k*) Solution-phase growth trajectory of toroidal Li₂O₂ in Li-O₂ battery. (*l*) Structural degradation including aggregation of Pt-Ni alloy catalysts during electrochemical potential cycling. (*m*) Structural evolution of Cu₂O nanocubes in CO₂ reduction reaction-relevant condition. (*n*) Individual rotavirus double-layered particles diffusing in liquids. (*o*) Formation process of block copolymer vesicles via amphiphilic self-assembly. Abbreviations: CE, counter electrode; IL, ionic liquid; LPTEM, liquid-phase transmission electron microscopy; PC, propylene carbonate; RE, reference electrode; WE, working electrode. Figures reproduced or adapted from the following with permission: (*b,e*) Reference 14, copyright 2012 American Association for the Advancement of Science (AAAS); (*c*) Reference 20, copyright 2010 AAAS; (*d*) Reference 27, copyright 2017 Springer Nature; (*f*) Reference 46, copyright 2016 AAAS; (*g*) Reference 49, copyright 2017 American Chemical Society (ACS); (*h*) Reference 62, copyright 2020 ACS; (*i*) Reference 70, copyright 2020 Springer Nature; (*j*) Reference 75, copyright 2015 ACS; (*k*) Reference 80, copyright 2019 ACS; (*l*) Reference 87, copyright 2019 Royal Society of Chemistry; (*m*) Reference 90, copyright 2020 Springer Nature; (*n*) Reference 92, copyright 2015 Royal Society of Chemistry; (*o*) Reference 102, copyright 2019 Springer Nature.

that the coalescence of presynthesized nanoparticles occurred concurrently with monomeric attachment (23). Au and Ag nanoparticle formation was achieved via a multistep process involving spinodal decomposition, formation of intermediate amorphous particles, and final crystallization (27) (**Figure 1d**). Studies to mechanistically understand coalescence have also been conducted via LPTEM (29–31). During coalescence, lattice alignment and structural reconstruction, known as the oriented attachment process, were observed for various nanoparticles (14) (**Figure 1e**). The coalescence behaviors dependent on the orientation between the nanoparticles and the surface ligands were also investigated (32–35).

Nanoparticle growth has been studied via LPTEM for more than a decade, and observations on the growth of oxides, alloys, core-shell nanoparticles, and multiply twinned nanoparticles as well as growth by galvanic replacement have been reported (29, 30, 36–38). Moreover, complex systems including heterogeneous core-shell growth and temperature-dependent growth behavior have been investigated directly in flow-type or temperature-controlled LPTEM (39, 40).

2.2. Nanoparticle Etching

Etching is an effective top-down approach for synthesizing nanomaterials with desired morphologies (41). Furthermore, wet chemical etching is an important step in semiconductor fabrication. LPTEM can investigate the overall and local site etching kinetics of nanomaterials in nanoscale (42). Both oxidative and reductive etching conditions for nanomaterials have been achieved in liquid cells. When the electron beam was irradiated onto a metal nanoparticle suspended in a metal halide solution of FeCl_3 , an oxidant from a reaction between Fe(III) and electron beam-generated $\text{Cl}_2^{\cdot-}$ radical etched the nanoparticle (43). Conversely, for aqueous solutions containing reducible oxides, the surface reduction of metal oxides by the electron beam resulted in reductive etching (44, 45).

Tracking the single-nanoparticle etching dynamics in LPTEM revealed the evolution of the kinetically driven morphology. Observations of Au nanorods and nanocube etchings in concentrated FeCl_3 solution confirmed the generation of nonequilibrium structures during etching that were intermediate nanocrystals composed of high-index surfaces (46) (**Figure 1f**). A similar study showed that Au nanocubes were transformed into different $\{hk0\}$ -faceted nanocrystals when the etchant concentration was controlled (47). These findings provided a fundamental background for the synthesis of complicated nanostructures via kinetically driven etching pathways.

It was also determined via LPTEM that the etching was highly sensitive to the local structure of the nanoparticles. The etching kinetics dependent on the position of the surface atoms were observed during Pd and Pt nanoparticle etching (48, 49) (**Figure 1g**). Analysis of CeO_2 nanocrystal etching revealed that etching depended significantly on surface structure (45). Other factors that caused the anisotropic etching of nanomaterials, such as surface ligands, diffusion rate, and atomic compositions, were also confirmed via LPTEM (42, 50, 51).

2.3. Nanoparticle Diffusion and Self-Assembly

Investigating nanoparticle motions in a nano-confined medium provides fundamental insights into nanoparticle applications in nano- and microfluidics (52). Particle motion in bulk medium is generally interpreted as Brownian motion. However, the nanoparticle motion analyzed in a confined system of LPTEM significantly deviated from Brownian motion, indicating the effect of the interaction between the nanoparticles and surroundings (53–56). Furthermore, in LPTEM, the measured diffusion coefficients of nanoparticles were typically in the range of 0.1 to 10 nm^2/s , at least six orders of magnitude smaller than that estimated in bulk medium using the Stokes–Einstein equation (12, 54, 57–59). LPTEM showed that nanoparticle diffusion dynamics depended

on liquid thickness, surrounding materials, and electron-beam irradiation (60, 61). Anomalous surface diffusion of nanoparticles in the Si/SiN_x platform was directly understood as a result of the electron beam-mediated electrostatic interaction between the nanoparticles and the window (53–59). In less-confined liquid cells, nanoparticles located several micrometers away from the SiN_x window exhibited Brownian motion with a diffusion coefficient similar to that estimated by the Stokes–Einstein equation (62) (**Figure 1b**).

When diffusing nanoparticles come into proximity with each other, attractive interparticle interactions induce nanoparticle self-assembly. The mechanism and the governing interaction of the self-assembly process were identified via LPTEM. LPTEM studies confirmed that the self-assembly of isotropically shaped nanoparticles can be driven by external convection (63) or nanoparticle–nanoparticle interactions (e.g., van der Waals, electrostatic, or magnetic dipole interactions) (64–66). Interestingly, characteristics of nonclassical crystallization, such as the coalescence of assembled nanoparticles and formation of disordered aggregates prior to periodic self-assembly, were observed during the self-assembly process (63, 66, 67). In addition, directional self-assembly behaviors were observed during the self-assembly of anisotropic nanoparticles, governed by their morphological anisotropy and surface ligand distribution (68, 69). Recently, observations of self-assembly dynamics at the 3D level have also been reported (70, 71). Ou et al. (70) observed the 3D assembly of Au nanoprisms in a thick liquid cell, elucidating the formation of an amorphous intermediate and the subsequent disorder-to-order transition that resulted in a micron-sized superstructure (**Figure 1t**).

2.4. Battery Systems

Understanding the structural changes during electrochemical reactions in battery systems is essential to improve battery performance. Huang et al. (20) proposed in situ electrochemical LPTEM with an open cell system composed of an ionic liquid electrolyte and directly observed the lithiation behavior of the SnO₂ nanowire. Open cell-type LPTEM has been used to investigate the phase transition and volume change of alloy-type nanowire anodes during lithiation/delithiation (72–74). However, the open cell approach can allow only a point contact between the electrode and electrolyte and therefore incompletely mimics the actual battery system in which the liquid electrolyte covers the electrode. Alternatively, the electrochemical LPTEM based on the Si/SiN_x platform fully immerses the electrode in the liquid electrolyte. In this platform, liquid-phase phenomena, such as solid-electrolyte interphase (SEI) formation and the reaction at the electrode–electrolyte interface during the charge/discharge process, were examined. For example, the formation dynamics, structure, and elemental composition of the SEI of various electrodes were analyzed (75–77). For Li metal batteries, Li plating/stripping dynamics and the formation dynamics of Li dendrites have been actively studied (75–78) (**Figure 1j**). Moreover, mechanisms of the surface- and solution-phase discharge reaction in the Li–O₂ battery system were investigated via LPTEM (79, 80) (**Figure 1k**).

2.5. Catalysis

Investigating structural change of catalysts in the reaction environment is crucial for identifying and avoiding the structural degradation of active sites. Whereas ex situ TEM techniques such as identical location TEM had been applied to analyze structural change in catalysts after reaction (81), LPTEM provided real-time monitoring of structural evolution of catalysts during the reaction. Si/SiN_x platforms equipped with multiple electrodes were used extensively to simultaneously investigate the structural changes in electrocatalysts along with their electrochemical

responses (82, 83). Furthermore, in situ monitoring of photocatalysts was also accomplished in LPTEM accompanied with a light source (84, 85).

The structural evolution of nanomaterials that catalyze electrocatalytic reactions, including the oxygen reduction reaction (ORR), oxygen evolution reaction (OER), and CO₂ reduction reaction (CO₂RR), was visualized successfully via LPTEM (86–90). For ORR catalysts such as Pt nanoparticles and Pt-*X* (*X* = Fe, Ni, etc.) alloy nanoparticles, LPTEM observations confirmed that degradation mechanisms depended on the catalyst location according to the electrode, alloy components, and operating voltage (86, 87) (**Figure 1l**). Structural change in the Co₃O₄ catalyst in the OER-active environment revealed that the amorphized cobalt oxide evolving during the OER cycle acted as the active site (88). In addition, the structural evolution of Cu₂O nanocubes under CO₂RR relevant environments was also observed via LPTEM (90) (**Figure 1m**).

2.6. Organic and Biomolecular Systems

Advances in performing LPTEM imaging under low-electron beam doses have stretched the capabilities of LPTEM in investigating soft materials. Understanding the structural diversity of individual macromolecules and how they develop into high-level structures in concentrated states remains a challenge. LPTEM has allowed direct observation of the intrinsic structure and dynamic behaviors of living and organic molecules. DNA strands, proteins, viruses, bacteria, and synthetic polymers were visualized in their native liquid state at the single-molecule level (10, 91–96) (**Figure 1n**). Use of flow-type liquid cells led to real-time observation of biomineralization by liquid mixing, enabling a mechanistic understanding of this process in iron oxide, calcium oxalate, and hydroxyapatite (97–99). These LPTEM studies revealed that the mineralization mechanisms involved the aggregation of prenucleated amorphous clusters and subsequent transformations into the crystalline phase. Additionally, reactions occurring in polymer solutions, such as polymerization, micellization, and self-assembly of synthetic polymers, were observed in LPTEM (100–102) (**Figure 1o**). These results provided mechanistic insight into the formation of functional polymeric nanostructures and important biological hierarchical structures. Furthermore, LPTEM was used to investigate the structural evolution of MOFs by directly monitoring their nucleation, growth, and phase transition (103, 104).

3. ELECTRON-BEAM CONTROL IN LPTEM

LPTEM observations always involve irradiation of a high-energy electron beam (typically >200 kV of acceleration voltage), which can affect solution chemistry and interact with suspended samples in many ways. For example, the electron beam can induce a structural change of suspended specimen, generate reactive species in the liquid, or alter the electronic state of transmitted materials. These electron-beam effects can be the origin of unwanted artifacts that prevent creating realistic environments during LPTEM imaging. This section briefly covers electron-beam chemistry in LPTEM that serves as a fundamental background to manipulate the electron beam-liquid interaction and properly design LPTEM experiments (10, 22, 105). In addition, recent approaches to control the electron-beam effect in various systems, by either suppressing or beneficially utilizing electron-beam effects, are presented.

3.1. Interactions Between the Electron Beam and Liquid-Phase Specimens

In LPTEM, the electron beam collides elastically or inelastically with the suspended sample, windows, and liquid media during transmission, altering the physicochemical state of the specimen in various ways (10, 22, 105, 106). Knock-on damage is the displacement or removal of individual atoms of the specimen via the high-angle elastic scattering of a primary electron. Knock-on

damage depends on the acceleration voltage and the atomic mass of the colliding atom. Moreover, subsequent inelastic scattering of primary electrons emits secondary electrons, accompanied by the energy transfer to the specimen. This induces radiolysis of the specimen, which consists of bond breakage, structural degradation, and mass loss. The extent of radiolysis is proportional to the cumulative electron-beam dose and becomes more severe under low-acceleration voltage conditions. In addition, for SiN_x windows, both elastic and inelastic scattering can create localized electrostatic charges (106). This charge imbalance induces local electric fields in the SiN_x windows, influencing nanoparticle motion (53, 54). The transferred energy during inelastic scattering can also generate heat (107) but is considered generally to be a minor artifact.

Particularly in LPTEM, the electron beam interacts with liquids and triggers radiolytic reactions. For pure water, the primary products of the radiolytic reactions involve $\text{OH}\cdot$, e^-_{aq} , $\text{H}\cdot$, H_2 , H_2O_2 , H_3O^+ , and $\text{HO}_2\cdot$ (108). Notably, after the incident electron-beam exposure, the primary species rapidly reaches steady-state concentration within microseconds. The species' steady-state concentration value depends highly on the electron-beam dose rate and initial chemical conditions. When the initial pH is greater than 3, the electron beam gradually shifts the pH to 3, making the solution acidic. Therefore, to accurately design an LPTEM experiment, one must first define the chemical environment of the liquid medium in electron beam-irradiated condition. For instance, Park et al. (25) calculated electron-beam effects for aqueous solutions containing chloride ions to understand the electron beam-dependent growth of Au nanoprisms (26).

3.2. Minimizing Unwanted Electron-Beam Effects for Imaging Beam-Sensitive Materials

Materials composed of light elements or weak chemical bonds or with low mechanical strength typically have poor tolerance to electron beams. This category includes polymers, biomolecules, MOFs, and electrolytes in battery systems. In particular, direct radiolysis causes substantial damage to these materials, leading to permanent changes in their local structures. Moreover, the reactive radiolytic species formed in a liquid environment can react with the suspended material, especially for materials with high surface exposure and biomolecules. Therefore, there is a growing need to mitigate electron-beam effects during LPTEM observation.

In general, radiation-sensitive materials exhibit substantial structural degradation via electron beam in the accumulated dose range of a few electrons to $\sim 10^2$ electrons per angstrom square (10, 105). The most straightforward way to minimize the electron-beam effect during LPTEM imaging is to perform the imaging under low-dose conditions. Dearnaley et al. (94) visualized the early stages of phage attachment to bacterial hosts in their native liquid environment over a total dose range of 10–20 $\text{e}^-/\text{\AA}^2$. Pulse irradiation of an electron beam is another way to reduce the cumulative dose, which Touve et al. (100) employed successfully to visualize polymerization-induced self-assembly of spherical micelles (**Figure 2a**). However, reducing the electron-beam dose deteriorates the signal-to-noise ratio (SNR) of the image, which could cause serious problems when imaging materials composed of light elements (109). In this case, direct electron detectors enable successful low-dose imaging with sufficient SNR (Section 4.1) (7).

Graphene can also remarkably reduce the electron-beam effect by suppressing radiation damage and scavenging hydroxyl radical species (95, 110, 111). Keskin & de Jonge (95) observed microtubule proteins in a GLC and demonstrated that graphene had a higher dose tolerance compared to cryo-TEM (**Figure 2b**). Other techniques to alleviate the electron-beam effect are the use of buffered saline, D_2O , or a radical scavenger to decrease the perturbation of solution chemistry by electron beam-generated species (96, 112–115) (**Figures 2c–e**). Synthetic polymers and organic materials are often soluble in organic solvents. Although some organic compounds,

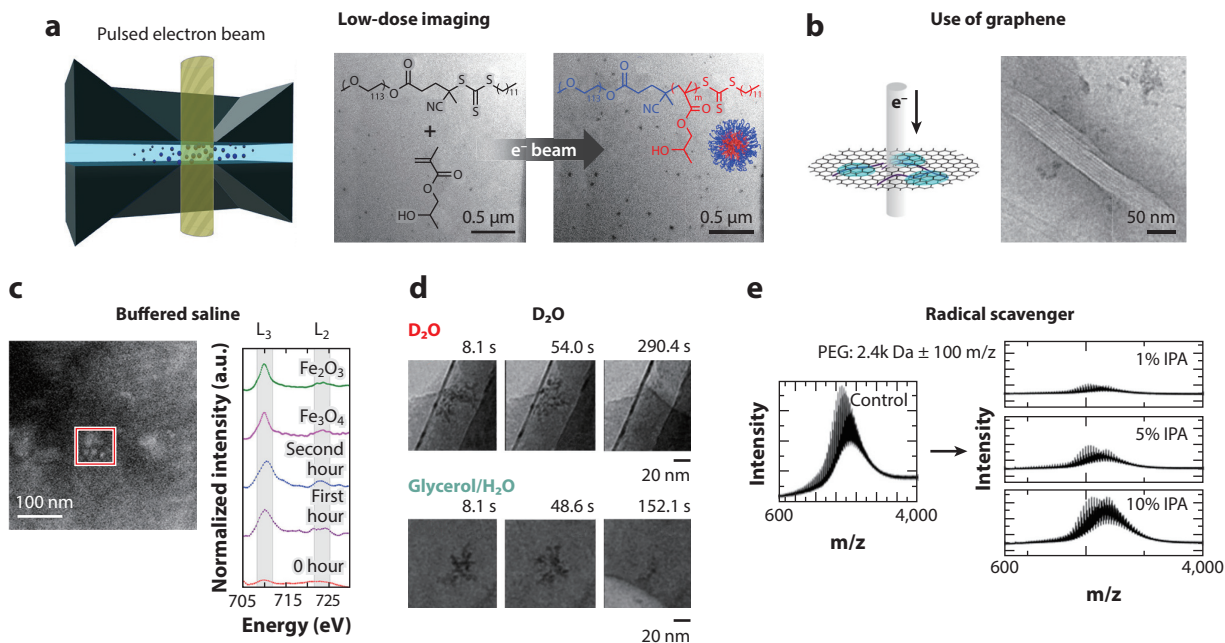


Figure 2

(*a–d*) Direct observation of (*a*) micelle formation under low-dose conditions with a pulsed electron beam, (*b*) microtubule proteins with graphene encapsulation, (*c*) ferritin biomineralization in buffered saline solution, and (*d*) polymer degradation in D₂O and in glycerol/H₂O solutions. (*e*) Mass spectrum of poly(ethylene glycol) before and after liquid-phase transmission electron microscopy imaging under 1%, 5%, and 10% 2-propanol cosolvent. Figures reproduced or adapted with permission from the following: (*a*) Reference 100, (*b*) Reference 95, (*c*) Reference 112, (*d*) Reference 96, and (*e*) Reference 113; copyright American Chemical Society.

including alcohols or formate anions, can act as an effective radical scavenger for OH \cdot and H \cdot (10, 114), further studies regarding electron-beam interactions with organic solvents are needed.

Along with various approaches to reduce electron-beam effects, validation processes using correlative experiments have also been conducted to quantify electron-beam damage and prove the absence of electron-beam effects (102, 116–118). He et al. (99) reported a mineralization pathway of hydroxyapatite in which classical and nonclassical nucleation coexist. By performing cryo-TEM experiments at different times and pH values, they elucidated that the electron beam did not alter the observed nucleation process. Touve et al. (119) used matrix-assisted laser desorption ionization imaging mass spectrometry to search for nondamaging dose conditions for observing peptide self-assembly.

3.3. Electron Beam-Guided Chemical Processes in LPTEM

Contrary to viewing the electron-beam effects as problematic, the electron beam can be used beneficially to control the chemical environment in LPTEM and stimulate the material dynamics of interest. Indeed, numerous LPTEM studies have examined nanoparticle growth by using solvated electrons to reduce metal precursors or nanoparticle etching by using an electron beam-generated etchant (Sections 2.1 and 2.2). Because the dose rate is directly related to the extent of the reactive species, tuning the dose rate can drive different growth kinetics and reveal important growth-determining factors (25, 26). For example, the relative proportion of different radiolysis products depends on the dose rate, which could direct the reaction toward either

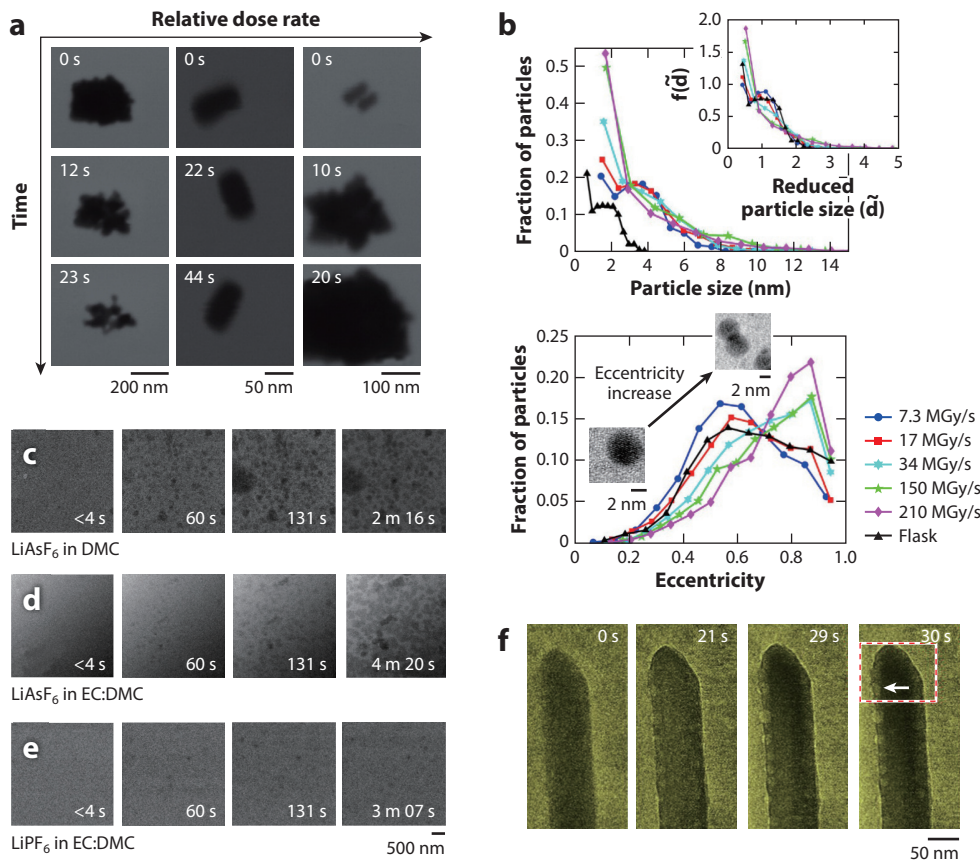


Figure 3

(a) Different transformation behavior of Au nanorods under different electron-beam dose rates. (b) Particle size distributions (*top*) and eccentricity distributions (*bottom*) of AuCu nanocrystals synthesized under different electron-beam dose rates. (c–e) Time-series degradation behavior of various Li-salt-containing electrolytes in LPTM. (f) Time-series LPTM images of hydrogen bubbles preferentially generated at the {110} surfaces of TiO₂ nanorod. Abbreviations: DMC, dimethyl carbonate; EC, ethylene carbonate; LPTM, liquid-phase transmission electron microscopy. Figures reproduced or adapted from the following with permission: (a) Reference 108, copyright 2014 American Chemical Society (ACS); (b) Reference 120, copyright 2021 ACS; (c–e) Reference 121, copyright 2014 ACS; (f) Reference 85, copyright 2019 Elsevier.

nanoparticle growth or etching (108) (**Figure 3a**). Recently, Wang et al. (120) investigated the different growth behaviors of AuCu nanocrystals from a metal thiolate precursor with varying dose rates from 7.3 to 210 MGy/s (**Figure 3b**). They elucidated that preserving the metal thiolate complex from oxidation was important to obtain nanocrystals with high Cu content. In addition, tuning the dose rate changes the distribution of charged functional groups on SiN_x windows, and thus different types of anomalous nanoparticle diffusion near the window were investigated directly when the dose rate was controlled between 2 and 49 e⁻/Å²·s (60).

Electron beam-guided chemical processes can create a model system to investigate Li-ion batteries and photocatalysis. Li-containing electrolytes are prone to electron beam-induced radiolysis. Interestingly, the mechanism and the product of electron beam-induced electrolyte degradation were quite similar to the breakdown in those of an actual battery system, featuring

LPTEM as a platform to test the stability of Li-containing electrolytes (121) (Figures 3c–e). In addition, Zheng and colleagues (84) used a low-dose electron beam as a light source and observed the facet-preferential generation of H₂ bubbles on TiO₂ nanorod, demonstrating beam-induced pseudophotocatalytic water splitting (Figure 3f).

4. HIGH-RESOLUTION LPTEM OF NANOMATERIAL DYNAMICS AND STRUCTURES IN LIQUID

Various nanoscale phenomena in chemical and biological engineering have been successfully visualized via LPTEM, as summarized in Section 2. However, underlying mechanisms of many of those studies require understanding nanomaterial structure and dynamics in liquid with atomic-scale resolution. With advances in liquid-cell fabrication techniques and TEM instruments, investigations of liquid-phase dynamics and structures of nanomaterials below subnanometer resolution are constantly being reported. This section addresses the instrumental requirements to achieve atomic resolution in LPTEM and introduces the scientific progress achieved using atomic-scale LPTEM imaging.

4.1. Prerequisites for Enhancing Resolution in LPTEM

The spatial resolution of LPTEM ($d_{overall}$) can be expressed as follows, where d_{Sch} is the resolution obtained at the Scherzer focus, d_{SNR} is the SNR-limited resolution, d_{TEMcc} is the chromatic aberration-limited resolution, and d_{blur} is the resolution affected by the electron-beam blurring (122):

$$d_{overall} = \sqrt{d_{Sch}^2 + d_{SNR}^2 + d_{TEMcc}^2 + d_{blur}^2}.$$

Because multiple factors determine $d_{overall}$, the criteria listed below should be considered collectively to enable atomic-resolution LPTEM imaging.

4.1.1. Reducing liquid cell dimensions. Theoretically, the phase contrast information on transmitted electrons that enables high-resolution imaging can be collected only when the sample thickness is smaller than half of the electron-mean free-path length (~170 nm in water, and under 200 kV acceleration voltage) (12, 122). Therefore, reducing the overall liquid cell thickness is the most straightforward method to achieve atomic resolution. Precise control of the thickness has been demonstrated via use of a specialized liquid cell design (123, 124). Thin and mechanically strong windows, including graphene, MoS₂, carbon film, and ultrathin (~10-nm) SiN_x, have been used to improve resolution (14, 35, 125, 126). Reducing the window thickness increases the SNR while suppressing electron-beam energy distribution broadening and blurring the electron beam, therefore reducing the d_{SNR} , d_{TEMcc} , and d_{blur} , respectively (13). However, window bulging owing to the pressure difference is severe for thin windows, which deteriorates the image resolution by increasing the liquid thickness (127). To avoid this, reducing the lateral dimensions of the window should be considered when using a thin window (13).

4.1.2. Application of direct electron detectors. The simplest way to improve SNR is to increase the electron-beam dose rate. However, as mentioned above, caution should be exercised when increasing the dose rate, as it can promote unwanted electron-beam effects. The application of direct electron detectors (DEDs) can significantly enhance the SNR without increasing dose rate (128, 129). Compared to conventional charge-coupled device detectors that sequentially convert collected electrons to photons and to electric signals, DEDs directly convert incoming electrons into electric signals, providing a high detective quantum efficiency value (above 0.2 at

Nyquist limit) (7). Furthermore, DED temporal resolution can reach below 1 ms. This fast data-acquisition ability enables the capturing of millisecond time-resolved liquid-phase dynamics with megapixel resolutions.

4.1.3. Application of spherical aberration-corrected TEM. Reducing the spherical aberration value (C_s) of the microscope directly reduces the d_{Scb} . Modern TEM equipped with C_s corrector can improve the image resolution to less than 0.08 nm (4). Therefore, LPTEM imaging with C_s -corrected TEM can be advantageous when the contribution of d_{Scb} is dominant over other resolution components, especially when imaging thin liquid specimens such as GLC.

4.1.4. Other imaging factors. Sample position in the liquid cell can also affect resolution. The best resolution can be achieved when the sample is placed in the bottom window because unwanted broadening of the electron beam is minimized (130). Increasing the acceleration voltage and controlling the dose rate can have a beneficial effect on reducing the chromatic aberration but should be adjusted carefully to minimize knock-on damage.

4.2. Atomic-Resolution Structural Dynamics in Liquid Observed via LPTEM

Atomic-scale structural dynamics of nanomaterials have been investigated successfully with the advancement of LPTEM. One of the major accomplishments is the atomic-scale identification of the nonclassical crystallization of nanoparticles. In classical crystallization theory, the supersaturation of atomic monomers directly forms crystalline nuclei (28). However, recent high-resolution LPTEM studies have revealed that the precipitation of the amorphous phase exists before crystallization. Investigation of the crystallization of Ni nanocrystals using GLC and aberration-corrected TEM showed that the amorphous phase was formed in the precursor solution and then crystallized (131) (**Figure 4a**). The presence of multiple crystallizations in single amorphous aggregates rationalized the formation of multi-grained nanocrystals via amorphous phase-mediated crystallization. Several studies have also reported the involvement of condensed atomic clusters during crystallization (132, 133). Dachraoui et al. (133) observed the crystallization of Au nanocrystals in atomic scale and confirmed the prenucleation of metal-rich condensed clusters prior to nanoparticle crystallization. By utilizing GLC combined with aberration-corrected scanning transmission electron microscopy (STEM), the image resolution at angstrom level was achieved in this study. The initially condensed clusters generated poorly crystallized nanoparticles. Crystallization was then preceded by the subsequent release and consumption of the condensed metal clusters, which resulted in the development of single-crystalline domains (**Figure 4b,c**).

During nanoparticle growth, important structural characteristics, including surface facets and grain boundaries, evolve in a single nanoparticle. However, the mechanism by which these structural features develop during nanoparticle growth is unclear. Liao et al. (125) used DED and an ultrathin SiN_x window to investigate Pt nanoparticle growth under millisecond temporal resolution and subnanometer spatial resolution (125). Pt nanoparticles had similar growth rates along different crystallographic directions of {100}, {011}, and {111} until they reached a critical size of ~ 5 nm (**Figure 4d,e**). After reaching a substantial size, the growth rates of individual surfaces differed owing to the facet-dependent mobility of the organic ligands. Song et al. (134) investigated the atomistic mechanisms of twin grain boundary formation (**Figure 4f-n**). To ensure sufficient spatial resolution, the nanoparticle solution was drop-casted on a TEM grid. The electron-beam irradiation on the unsealed Au nanoparticle solution decomposed the solvent molecules and induced an oriented attachment of Au nanoparticles. The absence of a top window enabled in situ imaging with atomic resolution. During the oriented attachment process, they identified two

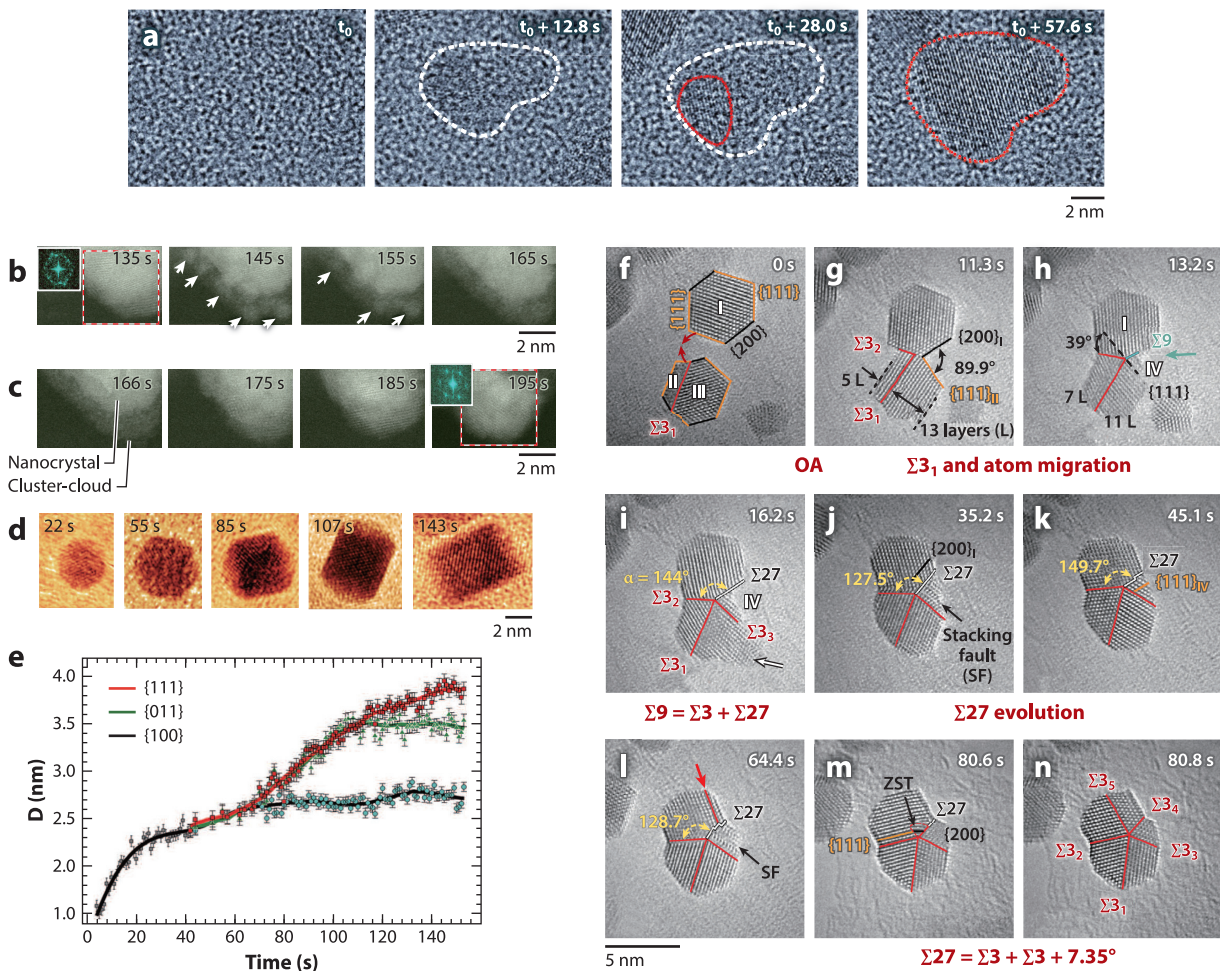


Figure 4

(a) Time-series transmission electron microscopy (TEM) images of a Ni nanocrystal crystallized via an amorphous phase-mediated pathway. (b,c) Liquid-phase scanning transmission electron microscopy (STEM) of the Au nanoparticle crystallization process. The polycrystalline Au (b) expels a condensed cluster cloud and (c) subsequently intakes the cluster cloud to generate single-crystalline nanocrystal. (d) Facet development of a Pt nanocube viewed along the [100] axis and (e) distances from the nanocrystal center to each surface according to the observed time. (f–n) Formation mechanism of fivefold-twinned Au nanoparticles by (f–h) oriented attachment, atom diffusion, and (i–n) formation and decomposition of high-energy grain boundary. Figures reproduced or adapted from the following with permission: (a) Reference 131, copyright 2019 American Chemical Society (ACS); (b,c) Reference 133, copyright 2021 ACS; (d,e) Reference 125, copyright 2014 American Association for the Advancement of Science (AAAS); (f–n) Reference 134, copyright 2020 AAAS.

different pathways to form fivefold-twinned nanocrystals: formation via decomposition of high-energy grain boundaries and via partial dislocation slipping.

In addition to the investigation of inorganic nanoparticles, high-resolution observation of soft material dynamics was also achieved via LPTM. Nagamanasa et al. (91) used GLC to image the dynamics of individual polymer molecules in aqueous solutions, without any labeling of metal species. The conformational motions of single polystyrene sulfonate, poly(ethylene oxide), and single-stranded DNA chains were visualized in GLC at the molecular level (91, 93, 96).

4.3. Three-Dimensional Atomic Structure of Single Particles in Liquids

Resolving the 3D location of individual atoms in a single particle is the ultimate step in determining its native structure. Although various methods had been used to investigate the 3D structure of nanomaterials (135–137), methods that enabled atomic-scale 3D structural analysis of nanomaterials in native liquid were limited. Cryo-TEM was recognized as a powerful method to obtain 3D structures of biological samples in a vitrified ice (138). Inspired by this Nobel Prize–awarded technique, recent LPTEM studies have verified the 3D atomic structure of individual particles in a liquid environment.

Kim et al. (139) developed a Brownian one-particle reconstruction method to determine the 3D atomic arrangement of a single Pt nanoparticle in a liquid. Herein, thousands of atomic-resolution TEM images of a Pt nanoparticle intrinsically rotating in GLC were obtained via employment of DED. The images were processed computationally to correct image drift, remove background scattering, and improve the SNR (140). Finally, a reconstruction algorithm was applied to generate 3D electron density maps of individual 8 Pt nanocrystals with an average atomic displacement of ± 19 pm (**Figure 5a,b**). Notably, nanoparticles synthesized from the same batch were heterogeneous in their structural features, including crystallinity, defects, dislocations, and strains. Furthermore, the interatomic distances increased gradually against the bulk lattice parameter as the atomic positions approached the surface, rationalized by surface ligand effects (**Figure 5c**). Although this 3D reconstruction analysis via cryo-TEM is applicable only to molecules that share identical structures, this method can obtain 3D atomic structures of individual nanoparticles that are structurally inhomogeneous.

Three-dimensional reconstruction of homogeneous biomolecules was also achieved in LPTEM, providing structural information related to the real-time dynamics of biomolecules. Jonaid et al. (141) used LPTEM to demonstrate the single-particle reconstruction of human adeno-associated viruses. Using DED, they performed low-dose imaging (cumulative dose of $20 \text{ e}^-/\text{\AA}^2$) to minimize structural degradation of samples and obtained high-resolution images (pixel resolution of 1.01 \AA) at high frame rates (40 fps) (**Figure 5d**). Single-particle LPTEM reconstruction with a structural resolution of 3.22 \AA revealed the detailed structure of a flexible surface loop that was unresolved in cryo-TEM-based structural identification (**Figure 5e**). The natural motions of biomolecules in the liquid phase could limit the resolution of their reconstructed structures, but the dynamic perspectives of liquid-suspended structures can be obtained only in LPTEM-based reconstruction, which will provide important discoveries related to their functional performance.

5. METHODS FOR QUANTITATIVE LPTEM

In general, nanomaterials are characterized in ensemble when bulk techniques such as spectroscopy are used. Compared to these ensemble analysis methods, LPTEM is inherently limited in the low sampling statistics because it is common to record single events or trajectories. Therefore, multiscale observation of chemical processes provided by LPTEM will be scientifically more acceptable when statistical information on the localized phenomena is obtained via unbiased data collection methods. To address this, advanced liquid cell designs have been developed to acquire plentiful LPTEM data sets under a defined liquid environment and with reproducible experimental methods. Moreover, software-based developments aim to objectively and rapidly process a large amount of in situ data sets through image-processing algorithms.

5.1. Reproducible and Massive Data Acquisition in LPTEM

Statistical and quantitative LPTEM requires the acquisition of excessive data sets in an identical liquid environment. However, conventional liquid cells based on GLC and Si/SiN_x platforms

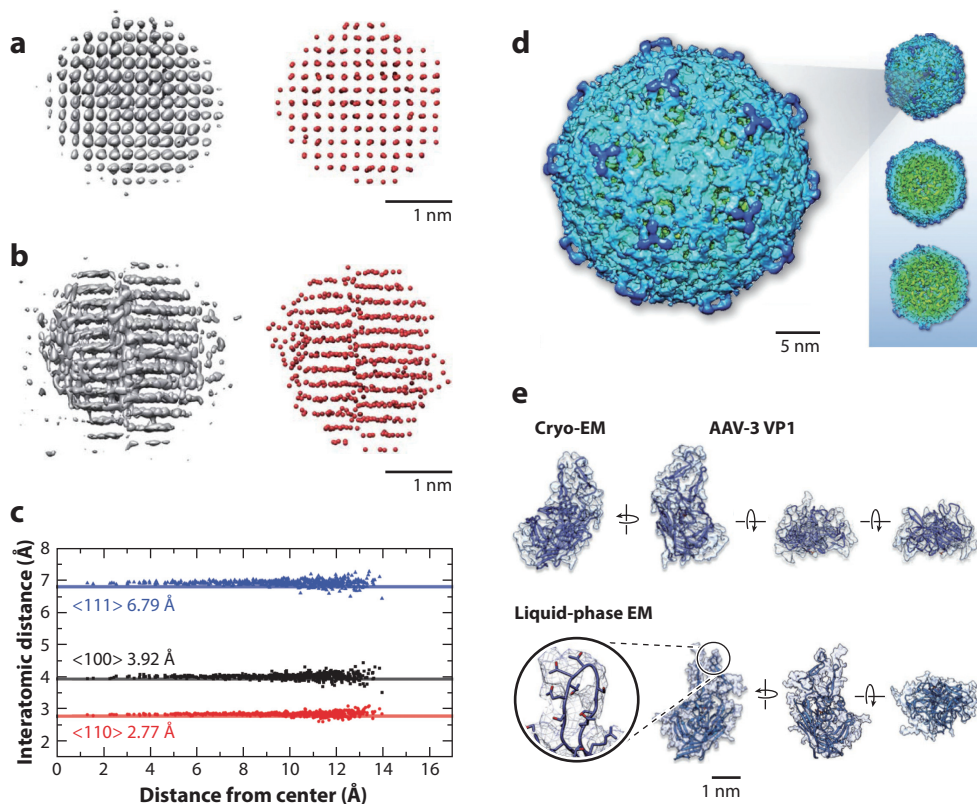


Figure 5

(*a,b*) Three-dimensional density maps (*left*) and corresponding atomic position maps (*right*) of (*a*) single-crystalline Pt nanocrystal and (*b*) nanocrystal with dislocation, obtained by Brownian one-particle reconstruction method. (*c*) Interatomic distances of Pt nanocrystal in panel *a*, according to various crystallographic directions. (*d*) Three-dimensional isosurface density maps of human AAV, obtained by single-particle LPTEM reconstruction. (*e*) Comparison of density maps and rotational views of individual capsid proteins obtained from cryo-transmission electron microscopy and LPTEM, showing the outer surface structure achieved with slightly higher resolution in solution than that in vitrified ice. Abbreviations: AAV, adeno-associated virus; EM, electron microscopy; LPTEM, liquid-phase transmission electron microscopy. Figures reproduced or adapted from the following with permission: (*a-c*) Reference 139, copyright 2020 American Association for the Advancement of Science; (*d,e*) Reference 141, copyright 2021 Wiley.

present some inherent problems regarding irregular geometry of liquid cells. In GLC, the liquid pockets typically are formed randomly with respect to population, size, and morphology. Therefore, generating a sufficient number of observable liquid pockets with consistent geometries is intrinsically difficult. Various strategies have been proposed to increase GLC reproducibility. Van Deursen et al. (142) presented a method to increase the low success rate of liquid pocket formation in GLC through loop-assisted graphene transfer methods. An alternative approach devised multi-chamber-type liquid cell designs with defined dimensions. These multi-chambered liquid cells consist of a uniform porous membrane and top/bottom window materials. The porous membrane is manufactured by drilling holes in various materials (e.g., SiN, BN, carbon) with defined thicknesses via microfabrication techniques (32, 143–147). Hutzler et al. (145) fabricated a SiN_x microwell-type liquid cell with graphene windows (**Figure 6a**). Kelly et al. (146) demonstrated

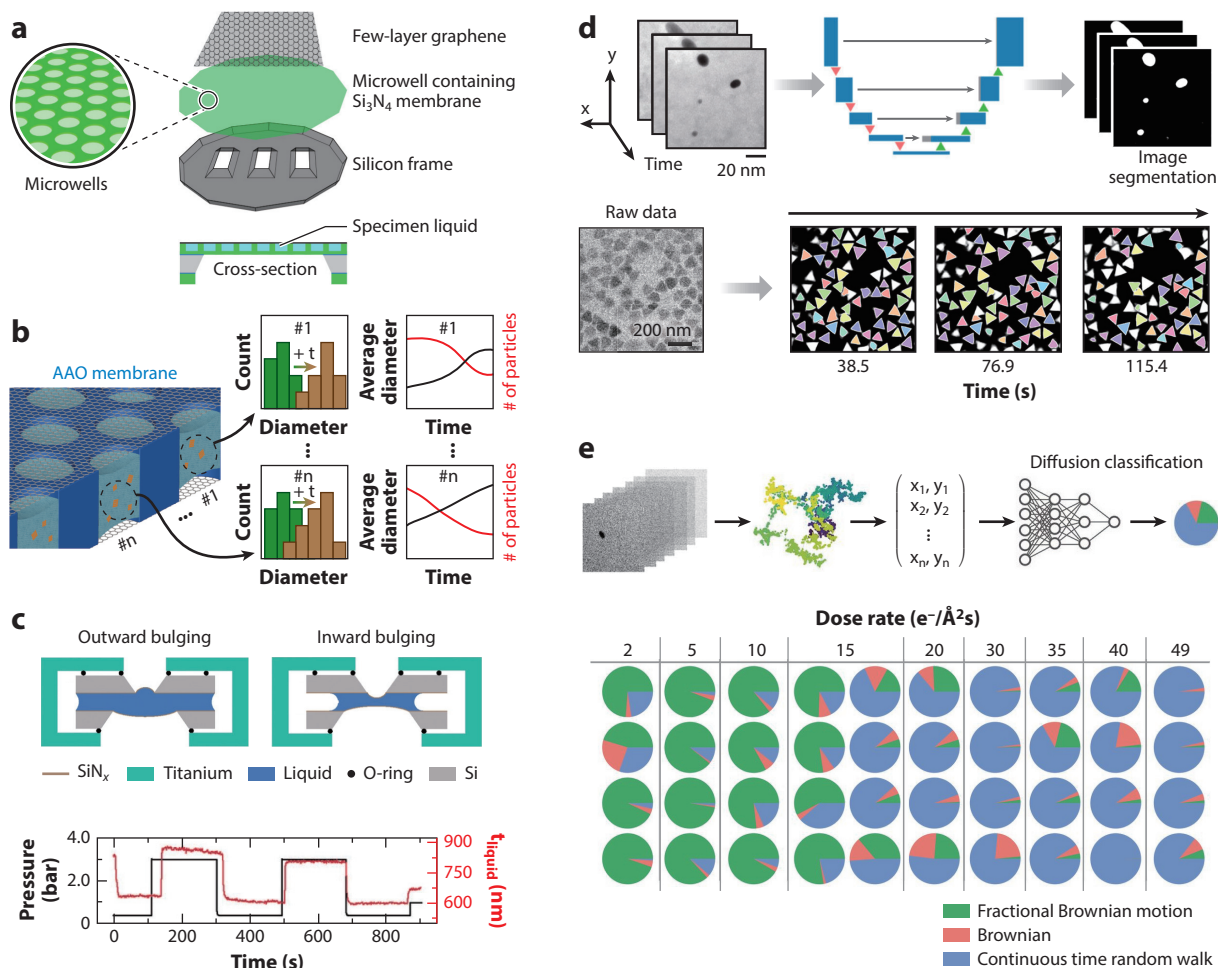


Figure 6

(*a,b*) Multi-chamber-type liquid cells with (*a*) Si_3N_4 and (*b*) anodic aluminum oxide membranes. (*c*) Pressure-based liquid thickness control in flow liquid cells. (*d,e*) Machine learning for precise and automated (*d*) in situ image segmentation and (*e*) nanoparticle diffusion classification. Abbreviation: AAO, anodic aluminum oxide. Figures reproduced or adapted from the following with permission: (*a*) Reference 145, copyright 2018 American Chemical Society (ACS); (*b*) Reference 147, copyright 2020 Wiley; (*c*) Reference 124, copyright 2021 Wiley; (*d*) Reference 151, copyright 2020 ACS; (*e*) Reference 60, copyright 2021 National Academy of Science.

elemental mapping with EELS and EDS using a GLC equipped with a patterned h-BN spacer. As an alternative to direct drilling methods, Lim et al. (147) used anodic aluminum oxide membranes to develop a graphene-based chamber-type liquid cell (**Figure 6b**). The large number of independent nanowells enabled repeatable observations of the same chemical reaction occurring in multiple chambers, allowing them to collect more than 80 in situ data for quantitative LPTM analysis (32).

For Si/ Si_3N_4 platforms, nonuniform liquid thickness owing to Si_3N_4 window bulging hinders the maintenance of constant experimental conditions. Wu et al. (124) reported a pressure-based liquid thickness control method using a flow system (**Figure 6c**). The internal pressure, determined by the Laplace and external pressures, can effectively control liquid thickness by adjusting window

bulging. Thus, by tuning the internal pressure, precise control of the liquid thickness in a range from 700 nm to as close to 0 nm was achieved. Despite remarkable advances in Si/SiN_x platforms, technological developments are still required to generate sufficient amounts of data sets when external stimuli such as heating and biasing are introduced.

5.2. Machine Learning–Based Data Analysis for LPTEM

Because modern LPTEM movies are obtained in thousands of megapixel frames for a prolonged time, tracking of the targeted material dynamics in LPTEM data sets is becoming an extensively time-consuming and labor-intensive process. Moreover, because multiple factors can contribute to nanoscale dynamics during LPTEM observation, effectively deconvoluting the factor that predominantly governs the observed phenomenon is not trivial. Therefore, an automated analysis method is desirable to avoid analyst subjectivity and to enable reliable data interpretation. In this sense, machine learning–based data-processing methods have gained considerable attention for characterizing nanoparticles in numerous in situ data sets.

Machine learning in image processing has been well applied in fields of facial recognition, biological image segmentation, and electron microscopy image analysis (148–150). For LPTEM, machine learning can be used to precisely extract the features of the target nanomaterial that are indiscernible owing to low SNR and image noise from the liquid. This process requires no artificial setting of values needed for image processing, and instead, model algorithms trained on diverse data sets mathematically determine the optimal values. Yao et al. (151) demonstrated automated image segmentation using neural network algorithms to analyze nanoparticle dynamics (**Figure 6d**). They trained the algorithms using fewer than 1,000 simulated LPTEM images. This training data set was generated for various polyhedral-shaped nanoparticles randomly placed on a SiN_x window under various extents of sample–electron interactions, dose rates, and noise levels. The trained algorithms clearly distinguished the nanoparticle edges from the background. Based on accurate image segmentation, the diffusion, etching, and self-assembly dynamics of the nanoparticles were analyzed precisely.

In addition to extracting nanoparticle morphology, machine learning can objectively classify the types of nanoscale dynamics observed in LPTEM. Jamali et al. (60) developed a deep learning–based method to investigate the anomalous motions of Au nanoparticles in SiN_x liquid cells (**Figure 6e**). The neural network model was trained on thousands of simulated short diffusion trajectories based on continuous-time random walk, fractional Brownian motion for anomalous diffusion, and Brownian motion for normal diffusion. With the trained model, the dominant diffusion processes for Au nanoparticles moving near the window were statistically classified according to the dose rate. Based on the results of electron beam–dependent diffusion motion of Au nanoparticles, the electron-beam effects on the SiN_x window and surrounding liquid medium were elucidated.

As indicated above, machine learning can be applied readily to improve original image quality, extract target object information or features, and classify changes in the tracked object's structural and dynamic properties. An excessive amount of high-quality training sets for a targeted system must be acquired for reliable machine-learning adaptation. Machine learning–based LPTEM analysis has great potential for application in various fields of chemical and biological engineering.

6. CONCLUSION

LPTEM is an in situ analysis method that directly resolves the structure, dynamics, and reactions of materials in liquids. Fundamental mechanisms underlying nanoparticle growth and etching, diffusion and self-assembly, catalysis, energy applications, and soft matter systems have been

elucidated via LPTEM. LPTEM is emerging as an indispensable tool to multidimensionally visualize structures and phenomena in their native states. Technological developments, including controlled electron-beam manipulations, improved spatial and temporal resolutions, and computational data acquisition and analysis methods, advance LPTEM as a reliable and quantitative method.

DISCLOSURE STATEMENT

The authors are not aware of any affiliations, memberships, funding, or financial holdings that might be perceived as affecting the objectivity of this review.

ACKNOWLEDGMENTS

This work is supported by the Institute for Basic Science (IBS-R006-D1), the National Research Foundation of Korea (NRF) grants funded by the Korean government (MSIT) (NRF-2020R1A2C2101871, NRF-2019M3E6A1064877, NRF-2021M3A9I4022936, NRF-2021M3H4A1A02049904, and NRF-2021M3H4A1A02045962), the Interdisciplinary Research Initiatives Programs by the College of Engineering and College of Medicine (Seoul National University, 2021), and the Creative-Pioneering Researchers Program through Seoul National University. The Institute of Engineering Research at Seoul National University provided research facilities for this work.

LITERATURE CITED

1. Zhang H, Gilbert B, Huang F, Banfield JF. 2003. Water-driven structure transformation in nanoparticles at room temperature. *Nature* 424(6952):1025–29
2. Prabhu N, Sharp K. 2006. Protein-solvent interactions. *Chem. Rev.* 106(5):1616–23
3. de Jonge N, Ross FM. 2011. Electron microscopy of specimens in liquid. *Nat. Nanotechnol.* 6(11):695–704
4. Ross FM, ed. 2016. *Liquid Cell Electron Microscopy*. Cambridge, UK: Cambridge Univ. Press
5. Liao HG, Zheng H. 2016. Liquid cell transmission electron microscopy. *Annu. Rev. Phys. Chem.* 67:719–47
6. Contarato D, Denes P, Doering D, Joseph J, Krieger B. 2012. High speed, radiation hard CMOS pixel sensors for transmission electron microscopy. *Phys. Procedia* 37:1504–10
7. Li X, Mooney P, Zheng S, Booth CR, Braunfeld MB, et al. 2013. Electron counting and beam-induced motion correction enable near-atomic-resolution single-particle cryo-EM. *Nat. Methods* 10(6):584–90
8. Williamson MJ, Tromp RM, Vereecken PM, Hull R, Ross FM. 2003. Dynamic microscopy of nanoscale cluster growth at the solid-liquid interface. *Nat. Mater.* 2(8):532–36
9. Kim BH, Yang J, Lee D, Choi BK, Hyeon T, Park J. 2018. Liquid-phase transmission electron microscopy for studying colloidal inorganic nanoparticles. *Adv. Mater.* 30(4):1703316
10. Parent LR, Gnanasekaran K, Korpanty J, Gianneschi NC. 2021. 100th anniversary of macromolecular science viewpoint: polymeric materials by *in situ* liquid-phase transmission electron microscopy. *ACS Macro Lett.* 10(1):14–38
11. Williams DB, Carter CB. 2009. *Transmission Electron Microscopy*. Boston: Springer
12. de Jonge N, Houben L, Dunin-Borkowski RE, Ross FM. 2019. Resolution and aberration correction in liquid cell transmission electron microscopy. *Nat. Rev. Mater.* 4(1):61–78
13. Li M, Knibbe R. 2020. A study of membrane impact on spatial resolution of liquid *in situ* transmission electron microscope. *Microsc. Microanal.* 26:126–33
14. Yuk JM, Park J, Ercius P, Kim K, Hellebusch DJ, et al. 2012. High-resolution EM of colloidal nanocrystal growth using graphene liquid cells. *Science* 336(6077):61–64
15. Ghodsi SM, Megaridis CM, Shahbazian-Yassar R, Shokuhfar T. 2019. Advances in graphene-based liquid cell electron microscopy: working principles, opportunities, and challenges. *Small Methods* 3(5):1900026

16. Lee C, Wei X, Kysar JW, Hone J. 2008. Measurement of the elastic properties and intrinsic strength of monolayer graphene. *Science* 321(5887):385–88
17. Koenig SP, Boddeti NG, Dunn ML, Bunch JS. 2011. Ultrastrong adhesion of graphene membranes. *Nat. Nanotechnol.* 6(9):543–46
18. Hauwiler MR, Ondry JC, Alivisatos AP. 2018. Using graphene liquid cell transmission electron microscopy to study *in situ* nanocrystal etching. *J. Vis. Exp.* 135:e57665
19. Koo K, Park J, Ji S, Toleukhanova S, Yuk JM. 2021. Liquid-flowing graphene chip-based high-resolution electron microscopy. *Adv. Mater.* 33(2):2005468
20. Huang JY, Zhong L, Wang CM, Sullivan JP, Xu W, et al. 2010. In situ observation of the electrochemical lithiation of a single SnO₂ nanowire electrode. *Science* 330(6010):1515–20
21. Pu S, Gong C, Robertson AW. 2020. Liquid cell transmission electron microscopy and its applications. *R. Soc. Open Sci.* 7(1):191204
22. Woehl TJ, Moser T, Evans JE, Ross FM. 2020. Electron-beam-driven chemical processes during liquid phase transmission electron microscopy. *MRS Bull.* 45(9):746–53
23. Zheng H, Smith RK, Jun YW, Kisielowski C, Dahmen U, Alivisatos AP. 2009. Observation of single colloidal platinum nanocrystal growth trajectories. *Science* 324(5932):1309–12
24. Woehl TJ, Evans JE, Arslan I, Ristenpart WD, Browning ND. 2012. Direct *in situ* determination of the mechanisms controlling nanoparticle nucleation and growth. *ACS Nano* 6(10):8599–610
25. Alloyeau D, Dachraoui W, Javed Y, Belkahlia H, Wang G, et al. 2015. Unravelling kinetic and thermodynamic effects on the growth of gold nanoplates by liquid transmission electron microscopy. *Nano Lett.* 15(4):2574–81
26. Park JH, Schneider NM, Grogan JM, Reuter MC, Bau HH, et al. 2015. Control of electron beam-induced Au nanocrystal growth kinetics through solution chemistry. *Nano Lett.* 15(8):5314–20
27. Loh ND, Sen S, Bosman M, Tan SF, Zhong J, et al. 2017. Multistep nucleation of nanocrystals in aqueous solution. *Nat. Chem.* 9(1):77–82
28. Lamer VK, Dinegar RH. 1950. Theory, production and mechanism of formation of monodispersed hydrosols. *J. Am. Chem. Soc.* 72(11):4847–54
29. Bronstein LM, Huang X, Retrum J, Schmucker A, Pink M, et al. 2012. Direction-specific interactions control crystal growth by oriented attachment. *Science* 336(6084):1014–18
30. Liao HG, Cui L, Whitlam S, Zheng H. 2012. Real-time imaging of Pt₃Fe nanorod growth in solution. *Science* 336(6084):1011–14
31. Jin B, Sushko ML, Liu Z, Jin C, Tang R. 2018. In situ liquid cell TEM reveals bridge-induced contact and fusion of Au nanocrystals in aqueous solution. *Nano Lett.* 18(10):6551–56
32. Bae Y, Lim K, Kim S, Kang D, Kim BH, et al. 2020. Ligand-dependent coalescence behaviors of gold nanoparticles studied by multichamber graphene liquid cell transmission electron microscopy. *Nano Lett.* 20(12):8704–10
33. Aabdin Z, Lu J, Zhu X, Anand U, Loh ND, et al. 2014. Bonding pathways of gold nanocrystals in solution. *Nano Lett.* 14(11):6639–43
34. Anand U, Lu J, Loh D, Aabdin Z, Mirsaidov U. 2016. Hydration layer-mediated pairwise interaction of nanoparticles. *Nano Lett.* 16(1):786–90
35. Zhu C, Liang S, Song E, Zhou Y, Wang W, et al. 2018. In-situ liquid cell transmission electron microscopy investigation on oriented attachment of gold nanoparticles. *Nat. Commun.* 9:421
36. Liang WI, Zhang X, Zan Y, Pan M, Czarnik C, et al. 2015. In situ study of Fe₃Pt-Fe₂O₃ core-shell nanoparticle formation. *J. Am. Chem. Soc.* 137(47):14850–53
37. Ma X, Lin F, Chen X, Jin C. 2020. Unveiling growth pathways of multiply twinned gold nanoparticles by *in situ* liquid cell transmission electron microscopy. *ACS Nano* 14(8):9594–604
38. Sutter E, Jungjohann K, Bliznakov S, Courty A, Maisonhaute E, et al. 2014. *In situ* liquid-cell electron microscopy of silver-palladium galvanic replacement reactions on silver nanoparticles. *Nat. Commun.* 5:4946
39. Wu J, Gao W, Wen J, Miller DJ, Lu P, et al. 2015. Growth of Au on Pt icosahedral nanoparticles revealed by low-dose *in situ* TEM. *Nano Lett.* 15(4):2711–15
40. Tan SF, Bisht G, Anand U, Bosman M, Yong XE, Mirsaidov U. 2018. *In situ* kinetic and thermodynamic growth control of Au-Pd core-shell nanoparticles. *J. Am. Chem. Soc.* 140(37):11680–85

41. Xia Y, Xiong Y, Lim B, Skrabalak SE. 2009. Shape-controlled synthesis of metal nanocrystals: Simple chemistry meets complex physics? *Angew. Chem. Int. Ed.* 48(1):60–103
42. Sun M, Tian J, Chen Q. 2021. The studies on wet chemical etching via in situ liquid cell TEM. *Ultramicroscopy* 231:113271
43. Crook MF, Laube C, Moreno-Hernandez IA, Kahnt A, Zahn S, et al. 2021. Elucidating the role of halides and iron during radiolysis-driven oxidative etching of gold nanocrystals using liquid cell transmission electron microscopy and pulse radiolysis. *J. Am. Chem. Soc.* 143(30):11703–13
44. Lu Y, Geng J, Wang K, Zhang W, Ding W, et al. 2017. Modifying surface chemistry of metal oxides for boosting dissolution kinetics in water by liquid cell electron microscopy. *ACS Nano* 11(8):8018–25
45. Sung J, Choi BK, Kim B, Kim BH, Kim J, et al. 2019. Redox-sensitive facet dependency in etching of ceria nanocrystals directly observed by liquid cell TEM. *J. Am. Chem. Soc.* 141(46):18395–99
46. Ye X, Jones MR, Frechette LB, Chen Q, Powers AS, et al. 2016. Single-particle mapping of nonequilibrium nanocrystal transformations. *Science* 354(6314):874–77
47. Hauwiler MR, Frechette LB, Jones MR, Ondry JC, Rotskoff GM, et al. 2018. Unraveling kinetically-driven mechanisms of gold nanocrystal shape transformations using graphene liquid cell electron microscopy. *Nano Lett.* 18(9):5731–37
48. Jiang Y, Zhu G, Lin F, Zhang H, Jin C, et al. 2014. In situ study of oxidative etching of palladium nanocrystals by liquid cell electron microscopy. *Nano Lett.* 14(7):3761–65
49. Wu J, Gao W, Yang H, Zuo JM. 2017. Dissolution kinetics of oxidative etching of cubic and icosahedral platinum nanoparticles revealed by *in situ* liquid transmission electron microscopy. *ACS Nano* 11(2):1696–703
50. Jiang Y, Zhu G, Dong G, Lin F, Zhang H, et al. 2017. Probing the oxidative etching induced dissolution of palladium nanocrystals in solution by liquid cell transmission electron microscopy. *Micron* 97:22–28
51. Chen L, Leonardi A, Chen J, Cao M, Li N, et al. 2020. Imaging the kinetics of anisotropic dissolution of bimetallic core-shell nanocubes using graphene liquid cells. *Nat. Commun.* 11:3041
52. Bocquet L, Charlaix E. 2010. Nanofluidics, from bulk to interfaces. *Chem. Soc. Rev.* 39(3):1073–95
53. Bakalis E, Parent LR, Vratsanos M, Park C, Gianneschi NC, Zerbetto F. 2020. Complex nanoparticle diffusional motion in liquid-cell transmission electron microscopy. *J. Phys. Chem. C* 124(27):14881–90
54. Parent LR, Bakalis E, Proetto M, Li Y, Park C, et al. 2018. Tackling the challenges of dynamic experiments using liquid-cell transmission electron microscopy. *Acc. Chem. Res.* 51(1):3–11
55. Woehl TJ, Prozorov T. 2015. The mechanisms for nanoparticle surface diffusion and chain self-assembly determined from real-time nanoscale kinetics in liquid. *J. Phys. Chem. C* 119(36):21261–69
56. Chee SW, Baraissov Z, Loh ND, Matsudaira PT, Mirsaidov U. 2016. Desorption-mediated motion of nanoparticles at the liquid-solid interface. *J. Phys. Chem. C* 120(36):20462–70
57. Lu J, Aabdin Z, Loh ND, Bhattacharya D, Mirsaidov U. 2014. Nanoparticle dynamics in a nanodroplet. *Nano Lett.* 14(4):2111–15
58. Verch A, Pfaff M, de Jonge N. 2015. Exceptionally slow movement of gold nanoparticles at a solid/liquid interface investigated by scanning transmission electron microscopy. *Langmuir* 31(25):6956–64
59. Chee SW, Anand U, Bisht G, Tan SF, Mirsaidov U. 2019. Direct observations of the rotation and translation of anisotropic nanoparticles adsorbed at a liquid-solid interface. *Nano Lett.* 19(5):2871–78
60. Jamali V, Hargus C, Ben-Moshe A, Aghazadeh A, Ha HD, et al. 2021. Anomalous nanoparticle surface diffusion in LCTEM is revealed by deep learning-assisted analysis. *PNAS* 118(10):e2018616118
61. Zheng H, Claridge SA, Minor AM, Alivisatos AP, Dahmen U. 2009. Nanocrystal diffusion in a liquid thin film observed by in situ transmission electron microscopy. *Nano Lett.* 9(6):2460–65
62. Yesibolati MN, Mortensen KI, Sun H, Broström A, Tidemand-Lichtenberg S, Mølhave K. 2020. Unhindered Brownian motion of individual nanoparticles in liquid-phase scanning transmission electron microscopy. *Nano Lett.* 20(10):7108–15
63. Park J, Zheng H, Lee WC, Geissler PL, Rabani E, Alivisatos AP. 2012. Direct observation of nanoparticle superlattice formation by using liquid cell transmission electron microscopy. *ACS Nano* 6(3):2078–85
64. Sutter E, Sutter P, Tkachenko AV, Krahn R, de Graaf J, et al. 2016. *In situ* microscopy of the self-assembly of branched nanocrystals in solution. *Nat. Commun.* 7:11213
65. Liu Y, Lin XM, Sun Y, Rajh T. 2013. In situ visualization of self-assembly of charged gold nanoparticles. *J. Am. Chem. Soc.* 135(10):3764–67

66. Powers AS, Liao HG, Raja SN, Bronstein ND, Alivisatos AP, Zheng H. 2017. Tracking nanoparticle diffusion and interaction during self-assembly in a liquid cell. *Nano Lett.* 17(1):15–20
67. Chen Q, Yuk JM, Hauwiller MR, Park J, Dae KS, et al. 2020. Nucleation, growth, and superlattice formation of nanocrystals observed in liquid cell transmission electron microscopy. *MRS Bull.* 45(9):713–26
68. Luo B, Smith JW, Ou Z, Chen Q. 2017. Quantifying the self-assembly behavior of anisotropic nanoparticles using liquid-phase transmission electron microscopy. *Acc. Chem. Res.* 50(5):1125–33
69. Liu C, Ou Z, Guo F, Luo B, Chen W, et al. 2020. “Colloid-atom duality” in the assembly dynamics of concave gold nanoarrows. *J. Am. Chem. Soc.* 142(27):11669–73
70. Ou Z, Wang Z, Luo B, Luijten E, Chen Q. 2020. Kinetic pathways of crystallization at the nanoscale. *Nat. Mater.* 19(4):450–55
71. Cepeda-Perez E, Doblas D, Kraus T, de Jonge N. 2020. Electron microscopy of nanoparticle superlattice formation at a solid-liquid interface in nonpolar liquids. *Sci. Adv.* 6(20):eaba1404
72. Wang CM, Li X, Wang Z, Xu W, Liu J, et al. 2012. In situ TEM investigation of congruent phase transition and structural evolution of nanostructured silicon/carbon anode for lithium ion batteries. *Nano Lett.* 12(3):1624–32
73. McDowell MT, Ryu I, Lee SW, Wang C, Nix WD, Cui Y. 2012. Studying the kinetics of crystalline silicon nanoparticle lithiation with in situ transmission electron microscopy. *Adv. Mater.* 24(45):6034–41
74. Gu M, Li Y, Li X, Hu S, Zhang X, et al. 2012. In situ TEM study of lithiation behavior of silicon nanoparticles attached to and embedded in a carbon matrix. *ACS Nano* 6(9):8439–47
75. Mehdi BL, Qian J, Nasybulin E, Park C, Welch DA, et al. 2015. Observation and quantification of nanoscale processes in lithium batteries by operando electrochemical (S)TEM. *Nano Lett.* 15(3):2168–73
76. Lee SY, Shanguan J, Alvarado J, Betzler S, Harris SJ, et al. 2020. Unveiling the mechanisms of lithium dendrite suppression by cationic polymer film induced solid-electrolyte interphase modification. *Energy Environ. Sci.* 13(6):1832–42
77. Gong C, Pu SD, Gao X, Yang S, Liu J, et al. 2021. Revealing the role of fluoride-rich battery electrode interphases by operando transmission electron microscopy. *Adv. Energy Mater.* 11(10):2003118
78. Zeng Z, Liang WI, Chu YH, Zheng H. 2014. In situ TEM study of the Li-Au reaction in an electrochemical liquid cell. *Faraday Discuss.* 176:95–107
79. Kushima A, Koido T, Fujiwara Y, Kuriyama N, Kusumi N, Li J. 2015. Charging/discharging nanomorphology asymmetry and rate-dependent capacity degradation in Li-oxygen battery. *Nano Lett.* 15(12):8260–65
80. Lee D, Park H, Ko Y, Park H, Hyeon T, et al. 2019. Direct observation of redox mediator-assisted solution-phase discharging of Li-O₂ battery by liquid-phase transmission electron microscopy. *J. Am. Chem. Soc.* 141(20):8047–52
81. Yang Y, Xiong Y, Zeng R, Lu X, Krumov M, et al. 2021. Operando methods in electrocatalysis. *ACS Catal.* 11(3):1136–78
82. Unocic RR, Sacci RL, Brown GM, Veith GM, Dudney NJ, et al. 2014. Quantitative electrochemical measurements using in situ ec-S/TEM devices. *Microsc. Microanal.* 20(2):452–61
83. Stricker EA, Ke X, Wainright JS, Unocic RR, Savinell RF. 2019. Current density distribution in electrochemical cells with small cell heights and coplanar thin electrodes as used in ec-S/TEM cell geometries. *J. Electrochem. Soc.* 166(4):H126–34
84. Yu S, Jiang Y, Sun Y, Gao F, Zou W, et al. 2021. Real time imaging of photocatalytic active site formation during H₂ evolution by in-situ TEM. *Appl. Catal. B* 284:119743
85. Yin Z-W, Betzler SB, Sheng T, Zhang Q, Peng X, et al. 2019. Visualization of facet-dependent pseudo-photocatalytic behavior of TiO₂ nanorods for water splitting using in situ liquid cell TEM. *Nano Energy* 62:507–12
86. Zhu GZ, Prabhudev S, Yang J, Gabardo CM, Botton GA, Soleymani L. 2014. In situ liquid cell TEM study of morphological evolution and degradation of Pt-Fe nanocatalysts during potential cycling. *J. Phys. Chem. C* 118(38):22111–19

87. Beermann V, Holtz ME, Padgett E, De Araujo JF, Muller DA, Strasser P. 2019. Real-time imaging of activation and degradation of carbon supported octahedral Pt-Ni alloy fuel cell catalysts at the nanoscale using *in situ* electrochemical liquid cell STEM. *Energy Environ. Sci.* 12(8):2476–85
88. Ortiz Peña N, Ihiwakrim D, Han M, Lassalle-Kaiser B, Carencu S, et al. 2019. Morphological and structural evolution of Co₃O₄ nanoparticles revealed by *in situ* electrochemical transmission electron microscopy during electrocatalytic water oxidation. *ACS Nano* 13(10):11372–81
89. Kim D, Kley CS, Li Y, Yang P. 2017. Copper nanoparticle ensembles for selective electroreduction of CO₂ to C₂–C₃ products. *PNAS* 114(40):10560–65
90. Arán-Ais RM, Rizo R, Grosse P, Algara-Siller G, Dembélé K, et al. 2020. Imaging electrochemically synthesized Cu₂O cubes and their morphological evolution under conditions relevant to CO₂ electroreduction. *Nat. Commun.* 11(1):3498
91. Nagamanasa KH, Wang H, Granick S. 2017. Liquid-cell electron microscopy of adsorbed polymers. *Adv. Mater.* 29(41):1703555
92. Varano AC, Rahimi A, Dukes MJ, Poelzing S, McDonald SM, Kelly DF. 2015. Visualizing virus particle mobility in liquid at the nanoscale. *Chem. Commun.* 51(90):16176–79
93. Wang H, Li B, Kim YJ, Kwon OH, Granick S. 2020. Intermediate states of molecular self-assembly from liquid-cell electron microscopy. *PNAS* 117(3):1283–92
94. Dearnaley WJ, Schleupner B, Varano AC, Alden NA, Gonzalez F, et al. 2019. Liquid-cell electron tomography of biological systems. *Nano Lett.* 19(10):6734–41
95. Keskin S, de Jonge N. 2018. Reduced radiation damage in transmission electron microscopy of proteins in graphene liquid cells. *Nano Lett.* 18(12):7435–40
96. Wang H, Hima Nagamanasa K, Kim YJ, Kwon OH, Granick S. 2018. Longer-lasting electron-based microscopy of single molecules in aqueous medium. *ACS Nano* 12(8):8572–78
97. Kashyap S, Woehl TJ, Liu X, Mallapragada SK, Prozorov T. 2014. Nucleation of iron oxide nanoparticles mediated by Mms6 protein *in situ*. *ACS Nano* 8(9):9097–106
98. Liu Z, Zhang Z, Wang Z, Jin B, Li D, et al. 2020. Shape-preserving amorphous-to-crystalline transformation of CaCO₃ revealed by *in situ* TEM. *PNAS* 117(7):3397–3404
99. He K, Sawczyk M, Liu C, Yuan Y, Song B, et al. 2020. Revealing nanoscale mineralization pathways of hydroxyapatite using *in situ* liquid cell transmission electron microscopy. *Sci. Adv.* 6(47):eaaz7524
100. Touve MA, Figg CA, Wright DB, Park C, Cantlon J, et al. 2018. Polymerization-induced self-assembly of micelles observed by liquid cell transmission electron microscopy. *ACS Cent. Sci.* 4(5):543–47
101. Early JT, Yager KG, Lodge TP. 2020. Direct observation of micelle fragmentation via *in situ* liquid-phase transmission electron microscopy. *ACS Macro Lett.* 9(5):756–61
102. Ianiro A, Wu H, van Rijt MMJ, Vena MP, Keizer ADA, et al. 2019. Liquid-liquid phase separation during amphiphilic self-assembly. *Nat. Chem.* 11(4):320–28
103. Lyu J, Gong X, Lee SJ, Gnanasekaran K, Zhang X, et al. 2020. Phase transitions in metal-organic frameworks directly monitored through *in situ* variable temperature liquid-cell transmission electron microscopy and *in situ* X-ray diffraction. *J. Am. Chem. Soc.* 142(10):4609–15
104. Liu X, Chee SW, Raj S, Sawczyk M, Král P, Mirsaidov U. 2021. Three-step nucleation of metal-organic framework nanocrystals. *PNAS* 118(10):e2008880118
105. Chen Q, Dwyer C, Sheng G, Zhu C, Li X, et al. 2020. Imaging beam-sensitive materials by electron microscopy. *Adv. Mater.* 32(16):1907619
106. Egerton RF, Li P, Malac M. 2004. Radiation damage in the TEM and SEM. *Micron* 35(6):399–409
107. Fritsch B, Hutzler A, Wu M, Khadivianazar S, Vogl L, et al. 2021. Accessing local electron-beam induced temperature changes during: *in situ* liquid-phase transmission electron microscopy. *Nanoscale Adv.* 3(9):2466–74
108. Schneider NM, Norton MM, Mendel BJ, Grogan JM, Ross FM, Bau HH. 2014. Electron-water interactions and implications for liquid cell electron microscopy. *J. Phys. Chem. C* 118(38):22373–82
109. Egerton RF. 2012. Mechanisms of radiation damage in beam-sensitive specimens, for TEM accelerating voltages between 10 and 300 kV. *Microsc. Res. Tech.* 75(11):1550–56
110. Cho H, Jones MR, Nguyen SC, Hauwiller MR, Zettl A, Alivisatos AP. 2017. The use of graphene and its derivatives for liquid-phase transmission electron microscopy of radiation-sensitive specimens. *Nano Lett.* 17(1):414–20

111. Koo K, Dae KS, Hahn YK, Yuk JM. 2020. Live cell electron microscopy using graphene veils. *Nano Lett.* 20(6):4708–13
112. Narayanan S, Shahbazian-Yassar R, Shokuhfar T. 2020. In situ visualization of ferritin biomineralization via graphene liquid cell-transmission electron microscopy. *ACS Biomater. Sci. Eng.* 6(5):3208–16
113. Korpanty J, Parent LR, Gianneschi NC. 2021. Enhancing and mitigating radiolytic damage to soft matter in aqueous phase liquid-cell transmission electron microscopy in the presence of gold nanoparticle sensitizers or isopropanol scavengers. *Nano Lett.* 21(2):1141–49
114. Woehl TJ, Abellan P. 2017. Defining the radiation chemistry during liquid cell electron microscopy to enable visualization of nanomaterial growth and degradation dynamics. *J. Microsc.* 265(2):135–47
115. Jokisaari JR, Hu X, Mukherjee A, Uskoković V, Klie RF. 2021. Hydroxyapatite as a scavenger of reactive radiolysis species in graphene liquid cells for *in situ* electron microscopy. *Nanotechnology* 32(48):485707
116. Wu H, Li T, Maddala SP, Khalil ZJ, Joosten RRM, et al. 2021. Studying reaction mechanisms in solution using a distributed electron microscopy method. *ACS Nano* 15(6):10296–308
117. Yamazaki T, Kimura Y, Vekilov PG, Furukawa E, Shirai M, et al. 2017. Two types of amorphous protein particles facilitate crystal nucleation. *PNAS* 114(9):2154–59
118. Dissanayake TU, Wang M, Woehl TJ. 2021. Revealing reactions between the electron beam and nanoparticle capping ligands with correlative fluorescence and liquid-phase electron microscopy. *ACS Appl. Mater. Interfaces* 13(31):37553–62
119. Touve MA, Carlini AS, Gianneschi NC. 2019. Self-assembling peptides imaged by correlated liquid cell transmission electron microscopy and MALDI-imaging mass spectrometry. *Nat. Commun.* 10(1):4837
120. Wang M, Leff AC, Li Y, Woehl TJ. 2021. Visualizing ligand-mediated bimetallic nanocrystal formation pathways with *in situ* liquid-phase transmission electron microscopy synthesis. *ACS Nano* 15(2):2578–88
121. Abellan P, Mehdi BL, Parent LR, Gu M, Park C, et al. 2014. Probing the degradation mechanisms in electrolyte solutions for Li-ion batteries by *in situ* transmission electron microscopy. *Nano Lett.* 14(3):1293–99
122. de Jonge N. 2018. Theory of the spatial resolution of (scanning) transmission electron microscopy in liquid water or ice layers. *Ultramicroscopy* 187:113–25
123. Keskin S, Kunas P, de Jonge N. 2019. Liquid-phase electron microscopy with controllable liquid thickness. *Nano Lett.* 19(7):4608–13
124. Wu H, Su H, Joosten RRM, Keizer ADA, van Hazendonk LS, et al. 2021. Mapping and controlling liquid layer thickness in liquid-phase (scanning) transmission electron microscopy. *Small Methods* 5(6):2001287
125. Liao HG, Zherebetsky D, Xin H, Czarnik C, Ercius P, et al. 2014. Facet development during platinum nanocube growth. *Science* 345(6199):916–19
126. Yang J, Choi MK, Sheng Y, Jung J, Bustillo K, et al. 2019. MoS₂ liquid cell electron microscopy through clean and fast polymer-free MoS₂ transfer. *Nano Lett.* 19(3):1788–95
127. Holtz ME, Yu Y, Gao J, Abruña HD, Muller DA. 2013. *In situ* electron energy-loss spectroscopy in liquids. *Microsc. Microanal.* 19(4):1027–35
128. Milazzo AC, Moldovan G, Lanman J, Jin L, Bouwer JC, et al. 2010. Characterization of a direct detection device imaging camera for transmission electron microscopy. *Ultramicroscopy* 110(7):741–44
129. Kühlbrandt W. 2014. The resolution revolution. *Science* 343(6178):1443–44
130. Zaluzec NJ. 2015. The influence of Cs/Cc correction in analytical imaging and spectroscopy in scanning and transmission electron microscopy. *Ultramicroscopy* 151:240–49
131. Yang J, Koo J, Kim S, Jeon S, Choi BK, et al. 2019. Amorphous-phase-mediated crystallization of Ni nanocrystals revealed by high-resolution liquid-phase electron microscopy. *J. Am. Chem. Soc.* 141(2):763–68
132. Jin B, Wang Y, Liu Z, France-Lanord A, Grossman JC, et al. 2019. Revealing the cluster-cloud and its role in nanocrystallization. *Adv. Mater.* 31(16):1808225
133. Dachraoui W, Keller D, Henninen TR, Ashton OJ, Erni R. 2021. Atomic mechanisms of nanocrystallization via cluster-clouds in solution studied by liquid-phase scanning transmission electron microscopy. *Nano Lett.* 21(7):2861–69
134. Song M, Zhou G, Lu N, Lee J, Nakouzi E, et al. 2020. Oriented attachment induces fivefold twins by forming and decomposing high-energy grain boundaries. *Science* 367(6473):40–45

135. Goris B, Bals S, Van Den Broek W, Carbó-Argibay E, Gómez-Graña S, et al. 2012. Atomic-scale determination of surface facets in gold nanorods. *Nat. Mater.* 11(11):930–35
136. Moody MP, Ceguerra AV, Breen AJ, Cui XY, Gault B, et al. 2014. Atomically resolved tomography to directly inform simulations for structure-property relationships. *Nat. Commun.* 5(1):5501
137. Ayyer K, Yefanov OM, Oberthür D, Roy-Chowdhury S, Galli L, et al. 2016. Macromolecular diffractive imaging using imperfect crystals. *Nature* 530(7589):202–6
138. Cheng Y. 2015. Single-particle cryo-EM at crystallographic resolution. *Cell* 161(3):450–57
139. Kim BH, Heo J, Kim S, Reboul CF, Chun H, et al. 2020. Critical differences in 3D atomic structure of individual ligand-protected nanocrystals in solution. *Science* 368(6486):60–67
140. Reboul CF, Heo J, Machello C, Kiesewetter S, Kim BH, et al. 2021. SINGLE: atomic-resolution structure identification of nanocrystals by graphene liquid cell EM. *Sci. Adv.* 7(5):eabe6679
141. Jonaid GM, Dearnaley WJ, Casasanta MA, Kaylor L, Berry S, et al. 2021. High-resolution imaging of human viruses in liquid droplets. *Adv. Mater.* 33(37):2103221
142. van Deursen PMG, Koning RI, Tudor V, Moradi MA, Patterson JP, et al. 2020. Graphene liquid cells assembled through loop-assisted transfer method and located with correlated light-electron microscopy. *Adv. Funct. Mater.* 30(11):1904468
143. Rasool H, Dunn G, Fathalizadeh A, Zettl A. 2016. Graphene-sealed Si/SiN cavities for high-resolution *in situ* electron microscopy of nano-confined solutions. *Phys. Status Solidi B* 253(12):2351–54
144. Wadell C, Inagaki S, Nakamura T, Shi J, Nakamura Y, Sannomiya T. 2017. Nanocuvette: a functional ultrathin liquid container for transmission electron microscopy. *ACS Nano* 11(2):1264–72
145. Hutzler A, Schmutzler T, Jank MPM, Branscheid R, Unruh T, et al. 2018. Unravelling the mechanisms of gold-silver core-shell nanostructure formation by *in situ* TEM using an advanced liquid cell design. *Nano Lett.* 18(11):7222–29
146. Kelly DJ, Zhou M, Clark N, Hamer MJ, Lewis EA, et al. 2018. Nanometer resolution elemental mapping in graphene-based TEM liquid cells. *Nano Lett.* 18(2):1168–74
147. Lim K, Bae Y, Jeon S, Kim K, Kim BH, et al. 2020. A large-scale array of ordered graphene-sandwiched chambers for quantitative liquid-phase transmission electron microscopy. *Adv. Mater.* 32(39):2002889
148. Li H, Lin Z, Shen X, Brandt J, Hua G. 2015. A convolutional neural network cascade for face detection. In *Proceedings of the 2015 IEEE Conference on Computer Vision and Pattern Recognition*, pp. 5325–34. New York: IEEE
149. Ziatdinov M, Dyck O, Maksov A, Li X, Sang X, et al. 2017. Deep learning of atomically resolved scanning transmission electron microscopy images: chemical identification and tracking local transformations. *ACS Nano* 11(12):12742–52
150. Moen E, Bannon D, Kudo T, Graf W, Covert M, Van Valen D. 2019. Deep learning for cellular image analysis. *Nat. Methods* 16(12):1233–46
151. Yao L, Ou Z, Luo B, Xu C, Chen Q. 2020. Machine learning to reveal nanoparticle dynamics from liquid-phase TEM videos. *ACS Cent. Sci.* 6(8):1421–30



Contents

Biosynthesis of Isonitrile- and Alkyne-Containing Natural Products <i>Antonio Del Rio Flores, Colin C. Barber, Maanasa Narayanamoorthy, Di Gu, Yuanbo Shen, and Wenjun Zhang</i>	1
Data-Driven Design and Autonomous Experimentation in Soft and Biological Materials Engineering <i>Andrew L. Ferguson and Keith A. Brown</i>	25
Flow Chemistry: A Sustainable Voyage Through the Chemical Universe en Route to Smart Manufacturing <i>Amanda A. Volk, Zachary S. Campbell, Malek Y.S. Ibrahim, Jeffrey A. Bennett, and Milad Abolbasani</i>	45
Transformation of Biopharmaceutical Manufacturing Through Single-Use Technologies: Current State, Remaining Challenges, and Future Development <i>Jasmin J. Samaras, Martina Micheletti, and Weibing Ding</i>	73
Interferometric Probing of Physical and Chemical Properties of Solutions: Noncontact Investigation of Liquids <i>Cornelia Eder and Heiko Briesen</i>	99
Airborne Transmission of SARS-CoV-2: Evidence and Implications for Engineering Controls <i>V. Faye McNeill</i>	123
Biopharmaceutical Manufacturing: Historical Perspectives and Future Directions <i>Alana C. Szkodny and Kelvin H. Lee</i>	141
Liquid-Phase Transmission Electron Microscopy for Reliable In Situ Imaging of Nanomaterials <i>Jongbaek Sung, Yuna Bae, Hayoung Park, Sungsu Kang, Back Kyu Choi, Joodeok Kim, and Jungwon Park</i>	167
Engineering Next-Generation CAR-T Cells: Overcoming Tumor Hypoxia and Metabolism <i>Torabito A. Gao and Yvonne Y. Chen</i>	193

Direct Air Capture of CO ₂ Using Solvents <i>Radu Custelcean</i>	217
Machine Learning–Assisted Design of Material Properties <i>Sanket Kadulkar, Zachary M. Sherman, Venkat Ganesan, and Thomas M. Truskett</i>	235
Advances in Manufacturing Cardiomyocytes from Human Pluripotent Stem Cells <i>Martha E. Floy, Fathima Shabnam, Aaron D. Simmons, Vijesh J. Bbute, Gyuhyung Jin, Will A. Friedrich, Alexandra B. Steinberg, and Sean P. Palecek</i>	255
Technological Options for Direct Air Capture: A Comparative Process Engineering Review <i>Xiaowei Wu, Ramanan Krishnamoorti, and Praveen Bollini</i>	279
The Critical Role of Process Analysis in Chemical Recycling and Upcycling of Waste Plastics <i>Scott R. Nicholson, Julie E. Rorrer, Avantika Singh, Mikhail O. Konev, Nicholas A. Rorrer, Alberta C. Carpenter, Alan J. Jacobsen, Yuriy Román-Leshkov, and Gregg T. Beckham</i>	301
Nanotherapeutics and the Brain <i>Andrea Joseph and Elizabeth Nance</i>	325
Blockchain Technology in the Chemical Industry <i>Xiaochi Zhou and Markus Kraft</i>	347
Optogenetics Illuminates Applications in Microbial Engineering <i>Shannon M. Hoffman, Allison Y. Tang, and José L. Avalos</i>	373
Machine Learning for the Discovery, Design, and Engineering of Materials <i>Chenru Duan, Aditya Nandy, and Heather J. Kulik</i>	405
Multilevel Mesoscale Complexities in Mesoregimes: Challenges in Chemical and Biochemical Engineering <i>Jianhua Chen, Ying Ren, Wen Lai Huang, Lin Zhang, and Jinghai Li</i>	431
Lessons from Biomass Valorization for Improving Plastic-Recycling Enzymes <i>Margarida Gomes, Yannick Rondelez, and Ludwik Leibler</i>	457
Medical 3D Printing: Tools and Techniques, Today and Tomorrow <i>Kelsey Willson and Anthony Atala</i>	481
Hydrogen Production and Its Applications to Mobility <i>Andres Gonzalez-Garay, Mai Bui, Diego Freire Ordóñez, Michael High, Adam Oxley, Nadine Moustafa, Paola A. Sáenz Cavazos, Piera Patrizio, Nixon Sunny, Niall Mac Dowell, and Nilay Shah</i>	501

Zeolitic Imidazolate Framework Membranes: Novel Synthesis
Methods and Progress Toward Industrial Use
*Dennis T. Lee, Peter Corkery, Sunghwan Park, Hae-Kwon Jeong,
and Michael Tsapatsis* 529

Errata

An online log of corrections to *Annual Review of Chemical and Biomolecular Engineering* articles may be found at <http://www.annualreviews.org/errata/chembioeng>